Spring 5-19-2017

A Computational Fluid Dynamics Study on Bidirectional Glenn Shunt Flow with an Additional Pulsatile Flow Through a modified Blalock-Taussig Shunt

Seda Aslan
saslan@uno.edu

A Computational Fluid Dynamics Study on Bidirectional Glenn Shunt Flow with an Additional Pulsatile Flow Through a modified Blalock-Taussig Shunt

A Thesis

Submitted to the Graduate Faculty of the
University of New Orleans
in partial fulfillment of the
requirements for the degree of

Master of Science
in
Mechanical Engineering

By

Seda Aslan

B.Sc. Selcuk University, 2014

May, 2017

Dedicated to my family

Acknowledgments

I would like to express my sincerest gratitude to my graduate advisor, Dr. Martin Guillot, for his invaluable guidance and support over the past two years. This work wouldn't have accomplished without his dedication and encouragement.

I am grateful to Dr. Robert and Dr. Nancy Ascuitto for their knowledge and support during this project.

I also wish to thank Dr. Kazim Akyuzlu and Dr. Ting Wang for serving on my thesis committee and for their constructive comments on this work.

Lastly, I wish to thank my family and friends for their support and encouragement during my graduate career.

Table of Contents

List of Figures

List of Tables

Nomenclature

ρ	Density (kg / m^3)
$\vec{u}$	Velocity vector ($u\hat{\imath} + v\hat{j} + w\hat{k}$) (m / s)
p	Pressure (Pa)
τ_{ij}	Shear stress tensor (Pa)
μ	Viscosity ($Pa \cdot s$)
μ_0	Zero shear viscosity ($Pa \cdot s$)
μ_∞	Infinite shear viscosity($Pa \cdot s$)
$\dot{\gamma}$	Shear rate (s^{-1})
λ	Time constant (s)
n	Power law index
$\overline{V}$	Averaged Velocity (m / s)
Q	Volumetric flow rate (m^3 / s)
A	Surface area (m^2)
e	Specific total energy (J / kg)
u	Internal energy (J / kg)
E	Energy (J)
$\dot{q}$	Heat (J)
$\dot{w}$	Work (J)
t	Time (s)
$\dot{m}$	Mass flow rate (kg / s)

Abstract

The blood flow through the Bidirectional Glenn shunt (BGS) and modified Blalock-Taussig shunt (mBTS) to the pulmonary arteries (PAs) was analyzed using Computational Fluid Dynamics. This study consisted of the steady and pulsatile cases. In Case 1, the results of blood flow through the BGS for the Newtonian and non-Newtonian viscosity models were compared. Case 2 focused on having an additional pulsatile blood flow through the mBTS using the non-Newtonian Carreau viscosity model. The geometries were created based on the angiograms.

In Case 1, boundary conditions to be specified at the inlets were obtained from the flow rate measurements via Doppler flow studies in children and young adults. The averaged velocities were obtained from these flow rates and specified as parabolic velocity profiles at the inlets. The average PA pressures were obtained from the catheterization data and specified at the outlets of the PA branches. In Case 2, boundary conditions at the same inlets were constant during the cardiac cycle. The pulsatile PA and aortic pressure tracings obtained from the catheterization data were specified at the outlets and mBTS inlet, respectively. A comparison is made between the first and second case results.

Keywords: Bidirectional Glenn Shunt, modified Blalock-Taussig Shunt

1 Introduction

A single ventricle heart disease is a type of congenital heart disease that occurs when either the right or the left ventricle of the heart is underdeveloped, smaller or missing a valve. These diseases are rare; only five out of 100,000 newborns have single ventricle heart disease. There are many type of single ventricle heart disease including: Hypoplastic Left Heart Syndrome, Tricuspid Atresia, and Mitral Atresia. Surgical managements, such as the Fontan procedure, are performed to provide a palliation to the patients with single ventricle heart disease. As a consequence of these managements, some unfavorable effects may arise within the cavopulmonary system. The aim of this study is to investigate these effects to provide a better understanding to treat these diseases.

1.1 Anatomy of a Healthy Heart

A healthy heart contains four chambers and four valves. The right and the left atriums are the two upper chambers, and the right and left ventricles are the two lower chambers of the heart. The right atrium is connected to right ventricle through the tricuspid valve. The oxygen depleted blood from the upper part of body through superior vena cava (SVC) and from the lower part of the body through inferior vena cava (IVC) reaches the right atrium, passes the tricuspid valve, and reaches the right ventricle. The pulmonary valve opens when the right ventricle pumpes the oxygen poor blood to the lungs through pulmonary arteries. Oxygen depleted blood is supplied with oxygen in the lungs. This oxygen rich blood is sent to the left atrium by passing through the pulmonary veins, then through mitral valve, it reaches to the left ventricle. The left

ventricle pumps the oxygen rich blood to the body through aorta. The valve that allows blood to flow from left ventricle to aorta is called aortic valve.

Figure 1.1 represents a healthy heart, indicating the veins, arteries, chambers, and valves in the heart. Blue and red flows represent oxygen depleted blood flow and oxygen rich blood flow, respectively.

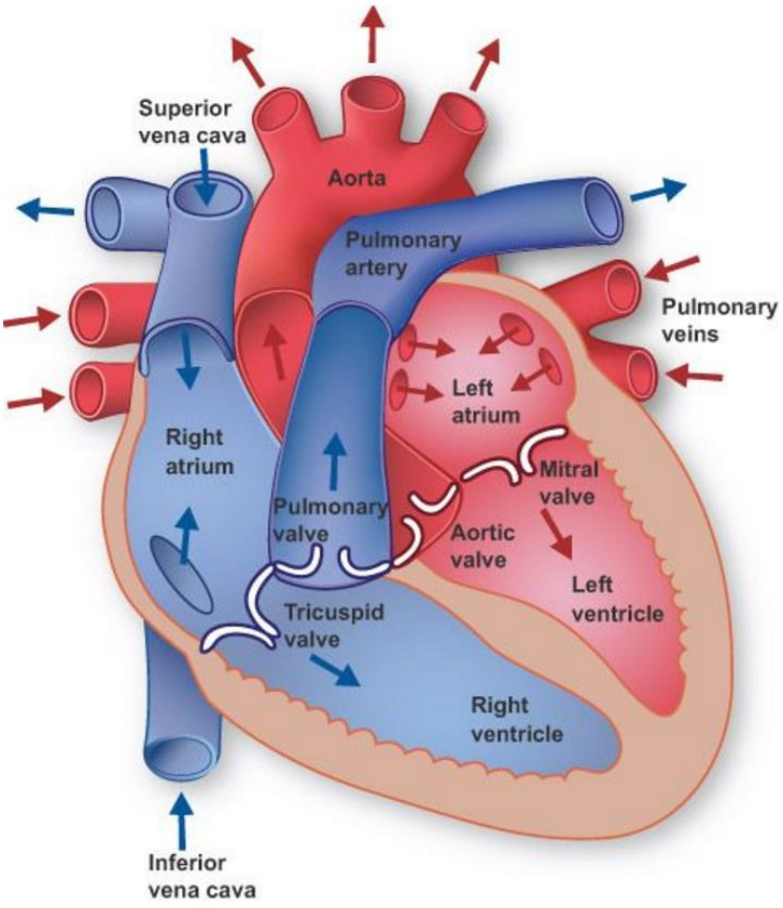

Figure 1.1: The schematics of a healthy heart showing the path of blood flow

1.2 Single Ventricle Heart Diseases

Hypoplastic Left Heart Sydrome: The left ventricle is not sufficiently developed to pump the blood through the aorta to the body. In the patients with hypoplastic left heart syndrome, the right ventricle supplies the blood flow to the lungs and the systemic system. Blood flows from the pulmonary arteries to the aorta through an opening called

patent ductus arteriosus, however this opening closes shortly after birth. Since the ductus arteriosus is the only way through oxygen rich blood is supplied to the systemic system, closing of it may cause immediate death. Medications are used to keep ductus arteriosus open until the surgical management is done.

Figure 1.2 shows the heart with hypoplastic left heart syndrome.

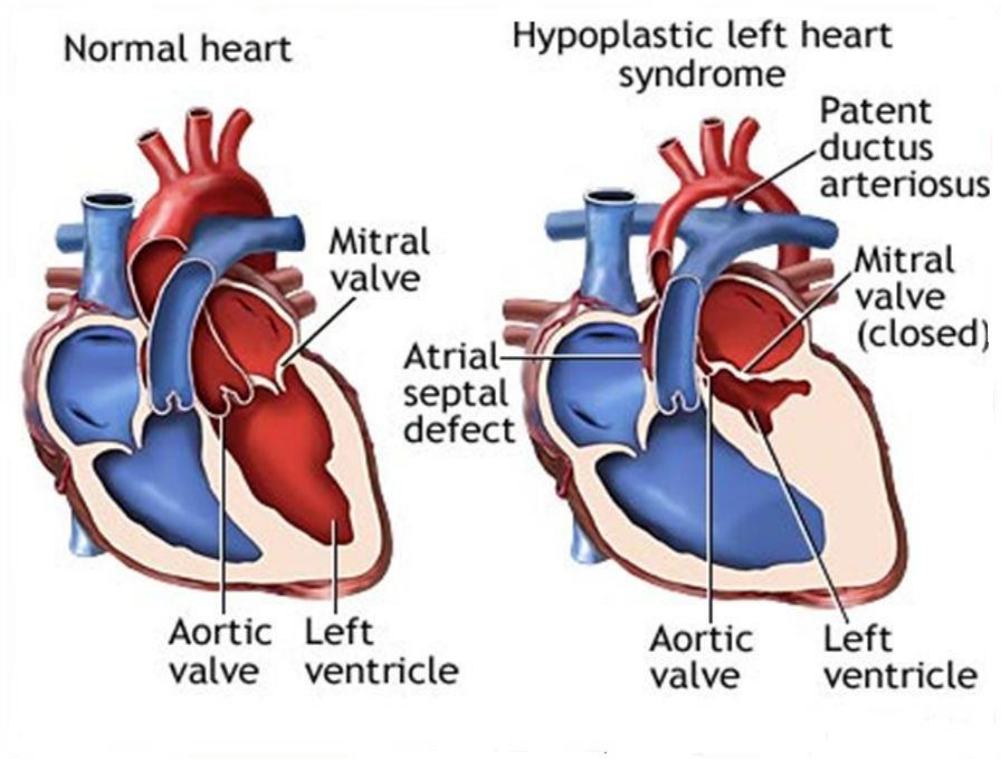

Figure 1.2: The comparison of a healthy heart and a heart with a hypoplastic left heart syndrome

Tricuspid Atresia: In patients with tricuspid atresia, the tricuspid valve is underdeveloped, therefore, the right ventricle is not developed since systemic venous blood can not flow to the right ventricle through the tricuspid valve. Atrial septal defect, opening between two atriums, allows oxygen-depleted blood to reach to the left atrium from the right atrium. Oxygen-depleted blood flows from left atrium to the left ventricle, mixes with oxygen-rich blood and the mixture is then pumped to the body through aorta. Another opening between the ventricles called ventricular septal defect, allows

the mixture of oxygen-depleted and oxygen rich blood to be pumped to the lungs. Patients with tricuspid atresia are cyanotic (blue baby syndrome) because of the low oxygen content of the blood that is circulates through the body. Figure 1.3 shows the heart with tricuspid atresia.

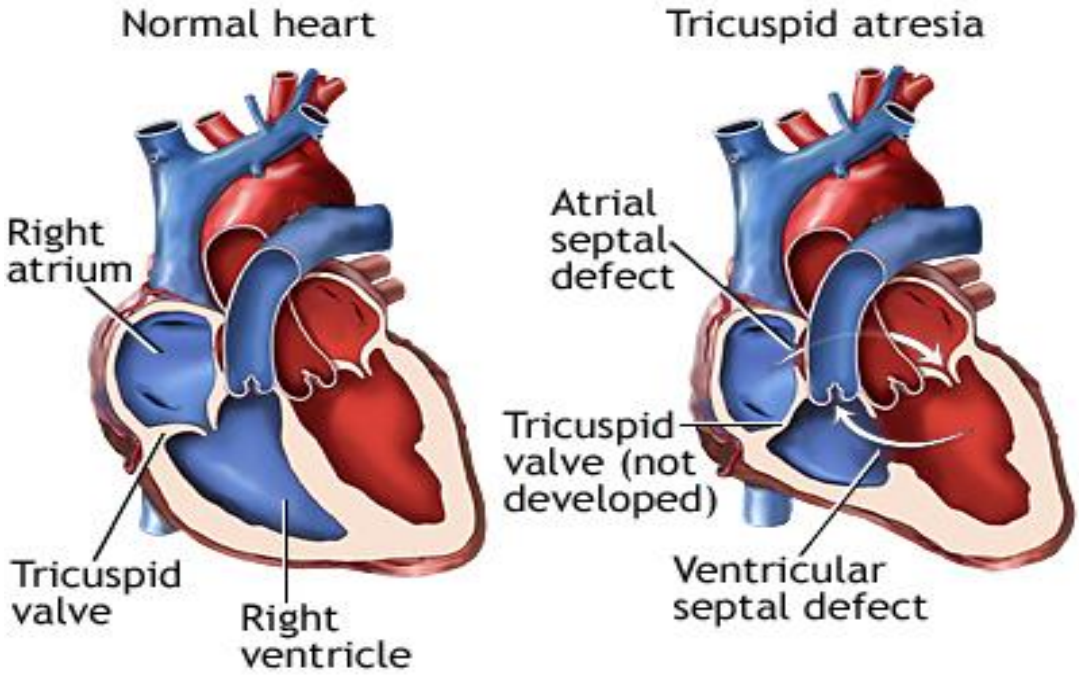

Figure 1.3: The comparison of a healthy heart and a heart with tricuspid atresia

1.3 Fontan Procedure

The Fontan Procedure is a surgical technique that is used in patients with single ventricle heart disease. The Fontan procedure includes three stages, and allows sytemic venous blood to flow directly to the lungs without passing through the right ventricle.

The first stage of the Fontan procedure is called the Norwood procedure that involves a shunt called Norwood-Sano shunt that is a tube which directs the blood flow from the right ventricle to the lungs through pulmonary arteries. This stage is done during the first weeks after birth to maintain blood flow from the heart to the body.

However, oxygen-depleted and oxygen-rich blood still mixes in the right ventricle before it is pumped to both the body and the lungs. Figure 1.4 represents a heart with Norwood-Sano Shunt.

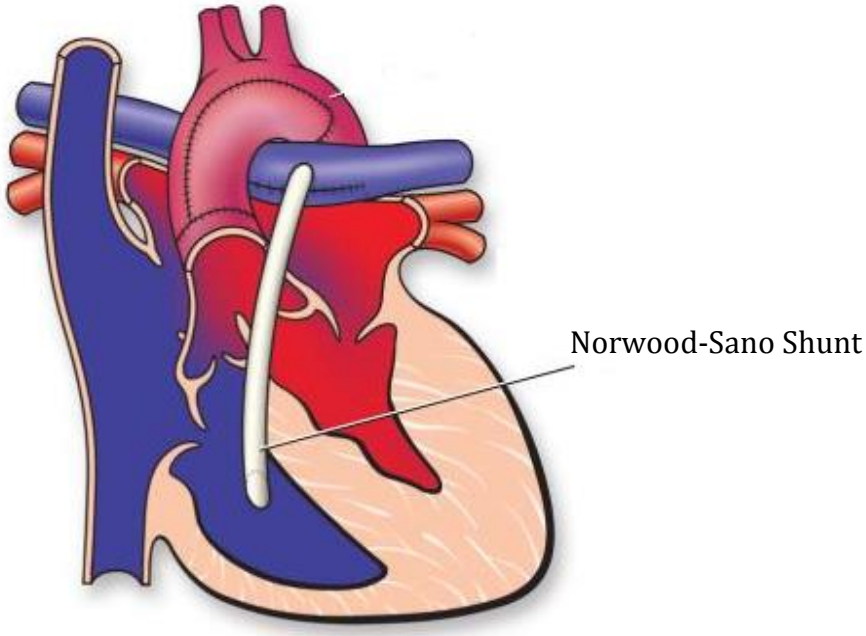

Figure 1.4: The schematics of a heart with Norwood-Sano shunt after the second stage of the Fontan Procedure

The second stage of the Fontan procedure is known as ''Bidirectional Glenn Shunt'' also called ''Hemi-Fontan''. This stage is applied four or five months after the baby is born. The ductus arterious and Norwood Sano shunt are removed in this stage. The SVC is detached from the right ventricle and is connected directly to the pulmonary arteries (PA) to supply oxygen-depleted blood flow to the lungs from upper part of the body. Since the Bidirectional Glenn Shunt (BGS) is the only source of blood flow to the PAs, in some patients the BGS is insufficient to maintain adequate systemic arterial oxygen saturation and PA growth. Therefore, it is often supplemented with a modified Blalock Taussig Shunt (mBTS).

The last stage, also called Fontan completion, redirects the blood flow from the inferior vana cava (IVC) to the lungs. After Fontan completion, oxygen-depleted and

oxygen-rich blood are completely separated since the oxygen-depleted blood from the body is redirected to the lungs through the connections of SVC and IVC to PAs. Figure 1.5 represents a heart after second and third stages of Fontan procedure.

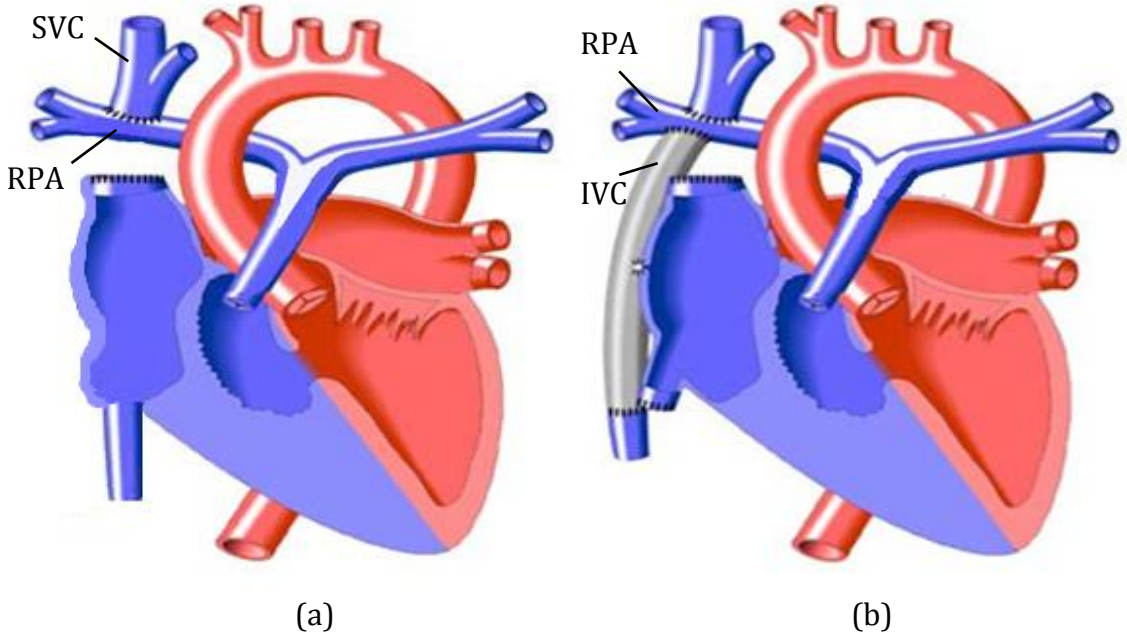

Figure 1.5: The schematics of a heart after (a) the BGS stage where the SVC is connected to the RPA and (b) the Fontan completion where the IVC is connected to the RPA

Figure 1.6 shows the mBTS connected to LPA in order to supply additional flow to the PAs after the BGS stage. The mBTS is removed once it provides an appropriate growth of PA's before the Fontan completion.

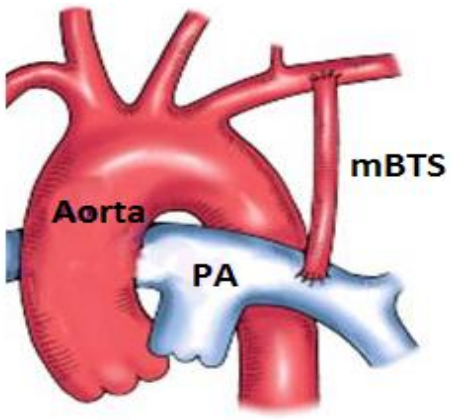

Figure 1.6: The mBTS connected to the LPA

1.4 Motivation

The BGS stage of Fontan procedure involves connecting the SVC to the RPA. Once this stage is completed, the viscous fluid flowing through the SVC is the only source of pulmonary blood flow. Therefore, in some patients with single ventricle heart diseases the BGS is not sufficient to maintain adequate systemic arterial oxygen saturation and pulmonary artery growth. In this case, Fontan completion is often delayed and pulmonary blood flow is maintained by existing BGS with an additional pulmonary blood flow from modified Blalock-Taussig Shunt (mBTS).

The mBTS provides a connection and supplies pulsatile blood flow from the aorta to the left pulmonary artery (LPA). However, this additional blood flow through the mBTS may cause following issues within the cavopulmonary system,

- Viscous fluid flow through the mBTS increase the systemic venous pressure,
- High velocity fluid flow through the mBTS creates secondary flow pattern within the PAs. The high wall velocity gradients as a consequence of secondary flow patterns result in increased wall shear stress magnitude to thrombogenic levels.
- High velocity viscous fluid flow advancing from the LPA disturbs the low velocity flow through SVC and increases the pressure in the SVC.
- Viscous fluid flow interactions in the PAs, between the BGS and mBTS deteriorate the mechanical energy loss.

1.5 Objectives of the study

This study aims to compare the hemodynamic effects and mechanical energy losses in the cavopulmonary system in the presence and in the absence of the mBTS.

The first part of the current study (Case 1) includes the BGS alone. It consist of connecting the SVC to the right pulmonary artery (RPA) in order to provide systemic blood flow to the lungs. In some patients, BGS is not sufficient to maintain adequate pulmonary artery growth because it is the only blood source to the PAs. Therefore, in the second part of the current study (Case 2), the BGS is supplemented with a mBTS in order to provide an additional blood flow to the PAs. The mBTS reroutes the pulsatile blood flow from the aorta to the LPA. Previous studies showed that additional pulsatile blood flow provides a sufficient pulmonary artery growth and arterial oxygen saturation [1]. On the other hand, high velocity blood flow from the mBTS may give rise to increased pressure in the SVC, and increased wall shear stress in the PAs. High wall shear stresses initiate endothelial cell function thereby activating thrombus formation which can cause sudden death [2].

The purpose of this study is to study the changes in WSS distributions and flow energy losses after supplementing a pulsatile mBTS flow to the steady BGS flow in order to provide a better understanding on thrombus formation and flow efficiencies in the system due to the inclusion of additional pulsatile flow from the mBTS.

2 Literature Review

The effects of wall shear stress on the arterial walls were addressed in various studies. Strony et al. [3] investigated the thrombus formations as a result of high wall shear stress and alterations in blood flow within a stenosed artery. Previously, Baumgartner et al. [4] and Sakariassen et al. [5] studied the impact of blood shear rate and the corresponding shear stress on thrombus formation and concluded that the increase in shear rate activated platelets and promoted growing thrombus, resulting in both increased platelet adhesion and cohesion. Holme et al [6] conducted an experimental study on the relationship between shear rate and thrombus formation in blood flow using a parallel-plate perfusion chamber device and presented that platelet activation increased at a shear rate of $10{,}500 s^{-1}$ which initiated thrombus formation.

Yoshida et al. [7] studied the role of additional pulmonary blood flow on BGS operation. Thirty eight patients who underwent BGS were enrolled in this study. Group A contained 29 patients who underwent BGS operation with additional blood flow that was controlled by the banding previously created Blalock Taussig shunt to sustain the pressure in the SVC equal or less than 16 mmHg (2133 Pa). Group B contained 9 patients who had only BGS to supply blood flow to PAs. The result of this study revealed that suitable additional pulmonary artery blood flow was beneficial to complete the Fontan procedure and pulmonary artery growth in patients with underdeveloped PAs. The impact of additional pulsatile blood flow in patients with BGS was investigated also by Ferns et al. [8]. The records of 103 selected patients were reviewed. Thirty three patients with pulsatile flow were considered in group A and 70 patients with non-pulsatile blood flow were considered in group B. The results of this study showed that there were significant differences in mean pulmonary artery pressure, which were 14

mmHg and 10 mmHg for group A and group B, respectively. Their results revealed that the additional pulsatile flow provided better growth in pulmonary arteries.

Migliavacca et al. [9] conducted a computational fluid dynamics study on the BGS flow with the pulsatile flow through the main PA. In this study, he investigated the flow distributions in the PAs. He assumed that the velocity profile at the inlet of the SVC was fully developed, the pressures at the outlets of the pulmonary arteries were uniform, and the geometry laid in the x-y plane. The results of this study indicated that the mean pressure in the SVC is slightly increased with pulsatile forward flow through the main pulmonary artery, and such a limited forward flow seemed beneficial for the perfusion of the lungs without excessive SVC hypertension. A schematic of the model that was used in this study is presented in Figure 2.1.

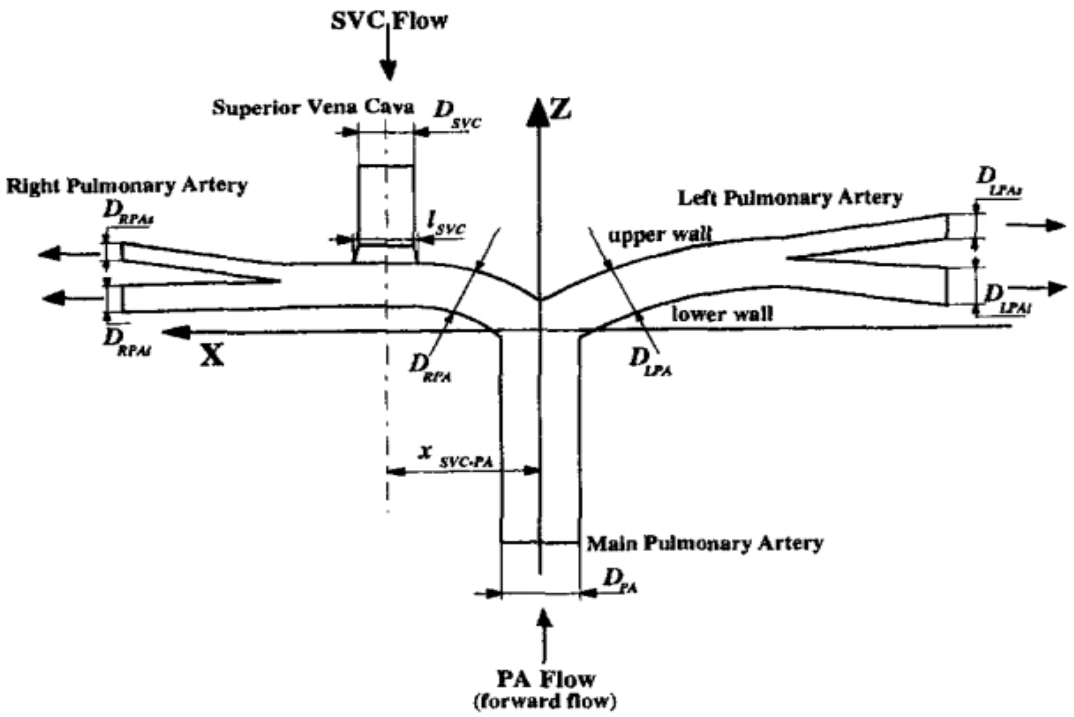

Figure 2.1: The schematic of the model that was used in the study of Migliavacca et al. [7]

Blood was assumed as Newtonian fluid in various studies [10, 11, 12.]. Gijsen et al. [13], compared the Newtonian and non-Newtonian (shear thinning) blood viscosity

models both experimentally and computationally. The shear thinning behavior of the blood was incorporated through the Carreau Yasuda model. The numerical results showed there was a significant difference in the measured velocity distributions of Newtonian and non-Newtonian fluid. The non-Newtonian fluid showed flattened axial velocity profile due to its shear thinning behavior.

Cho et al. [14] conducted a numerical investigation on the effects of non-Newtonian blood viscosity on flows in a diseased arterial vessel. He concluded that the Newtonian assumption of blood viscosity was reasonable when the shear rates were higher than 200 s^{-1}. In this study, various constitutive models were used for modeling the non-Newtonian viscosity of blood. The relation between shear rate and blood viscosity was presented at the percentage blood hematocrit (the ratio of the volume of the red blood cells to the total volume of the blood) at 33-45 for Cross, Carreau and Casson models. The blood viscosity vs. shear rate curve indicated that when shear rates were higher than 200 s^{-1}, the shear stress remained constant. In Cho's study the curve fitting parameters for Carreau model were, λ=3.313s, n = 0.3568, μ_0=0.56poise, μ_{inf}=0.0345poise.

These studies lead to the present work on the identification of the appropriate boundary conditions and fluid viscosity model.

3 Methods

In this research 3D idealized geometric model was created based on the angiograms using Autodesk Inventor software [15]. Ansys meshing was utilized to mesh the geometries that were used in case one and case two.

The Ansys Fluent software [16] using Finite volume method (FVM) was utilized to solve 3D incompressible Navier Stokes equations, for both case one and case two, based on velocity and pressure boundary conditions determined from Doppler flow studies and in vivo catheterization measurements.

Generally the LPA has a slightly smaller diameter than the RPA as it is seen in Figure 3.1. For the idealized model, it is assumed that both arteries have the same diameter and length, and their symmetry axises lie in x-y plane. Both PAs are 9 mm in diameter and 24.5 mm in length with the first order branches of 4.5mm and 7mm diameter. The vessel sizes are based on reported values for children and young adults [17] as BGS 12.5 mm- 39.5 mm, Right Innominate Vein (R-INV) 9.8mm -10 mm, L-INV 9.8mm-32 mm, where first number represents diameter while second represents the length. Additionally, subclavian and internal jugular veins, which drain blood to the innominate veins were included in the domain in order to have more realistic flow in the BGS and provide adequate boundary conditions, instead of assuming a parabolic velocity profile at the inlet to the SVC as it was specified in the study of Migliavacca et al. [9]. Appendix 1 consists of a comparison of contour and vector plot of velocity distribution at the axis of the BGS in the absence and presence of the veins provide blood flow to the SVC. The BGS (SVC), right internal jugular vein (R-IJV), right subclavian vein (R-SCV), left internal jugular vein (L-IJV) and left subclavian vein (L-SCV) diameters and lengths were determined from Doppler flow studies in children

[18]. The diameters and lengths of the R-IJV, R-SCV, L-IJV and L-SCV are 6.9mm-20mm, 4.9mm-20mm, 6.9mm-20 mm and 4.9mm-20mm, respectively. In Case 2, which includes time-dependent mBTS flow, the shunt was connected in the middle of the LPA. The mBT shunt is 4 mm in diameter and 40 mm in length. The distance between the axis of the mBT shunt and the axis of the BGS is 27 mm. Table 3.1 shows the sizes of the major systemic vessels with the flow rates.

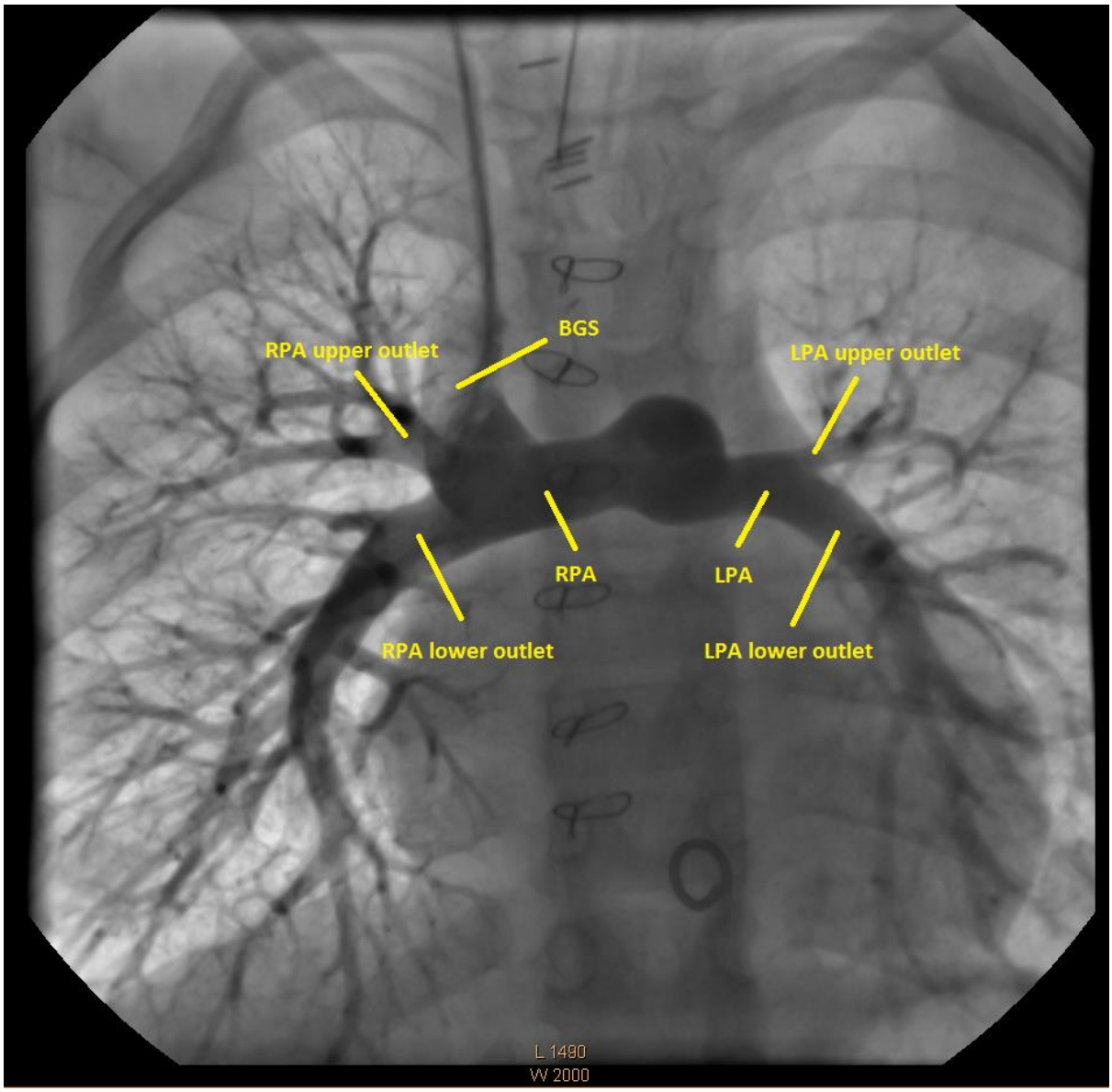

Figure 3.1: Front view of an angiogram

Table 3.1: Major systemic veins providing blood flow to the SVC. Values are for an approximately 3 year old (BS 0.65 m2)

Vessel	Diameter(mm)	Length (mm)	Flow Rate (L/min)
R-SCV	4.9	20	0.19
R-IJV	6.9	20	0.28
L-SCV	4.9	20	0.22
L-IJV	6.9	20	0.31
R-INV	9.8	10	0.47
L-INV	9.8	32	0.53
SVC	12.5	39	1.0

The governing differential equations require boundary conditions be applied at all domain boundaries. The inlet of the mBTS is located in the left common carotic artery or left subclavian artery, which are the branches originated in the aorta. The aorta is a very large vessel with very low velocities therefore, kinetic energy is neglected, and the total pressure is assumed to be equal to the static pressure. The time dependent static pressure was measured in the aorta via catheterization, and is applied as the total pressure boundary condition at the inlet of the mBTS.

The rates of the flow distributions in the L-INV and R-INV, L-SCV and L-IJV and R-SCV and R-IJV are obtained from Doppler studies [18] and scaled to yield the volumetric flow rate of 1L/min in the BGS. In order to apply more realistic boundary conditions at the L-SCV and L-IJV and R-SCV and R-IJV inlets, these veins are extended to the entrance length to yield fully developed flows at the inlets of these veins for the first simulation. The averaged velocities are determined from these flow rates and specified at the inlets of extended veins. The same veins are shortened to actual lengths and the velocity

profiles at these distances obtained from the first simulation are specified at the inlets for the remainder of the simulations.

In Case 2, same inlet velocity profiles specified at the inlets are constant during the cardiac cycle. The time dependent static pressure was measured in the PAs and it is assumed they are identical in the branches. This measured pulsatile pressure tracing is specified as static pressure boundary condition at the outlets. The time dependent aortic and pulmonary artery pressure traces to be specified at the mBTS inlet, and LPA and RPA outlets is shown in section 4.5.5. The summary of simulations included in this study is shown in Table 3.2.

Table 3.2: Summary of simulations included in this study

	Simulations
Case 1 (BGS)	Geometry 1- Steady, Newtonian
	Geometry 1- Steady, non-Newtonian
Case 2 (BGS with mBTS)	Geometry 2- Pulsatile, non-Newtoninan

4 Mathematical Model

In this chapter, assumptions and equations used in the current study are presented.

Assumptions

This study assumes,

- 3 D Domain
- Laminar Fluid Flow
- Incompressible and Non Newtonian Fluid
- Gravitational force is negligible
- Walls are rigid and impermeable
- No external forces

Governing Differential Equations

Viscous fluid flow is governed by conservation of mass and conservation of momentum equations also called Navier-Stokes equations.

Continuity (conservation of mass) equation in vector form can be written as

$$\frac{\partial \rho}{\partial t} + \nabla \cdot (\rho \vec{u}) = 0 \tag{4.1}$$

For an incompressible fluid equation above reduces to

$$\nabla \cdot \vec{u} = 0 \tag{4.2}$$

Navier Stokes equations (conservation of momentum) in vector form can be written as

$$\rho \frac{D\vec{u}}{Dt} = -\nabla p + \rho \vec{g} + \nabla \cdot \tau_{ij} \tag{4.3}$$

External forces and gravitational acceleration are neglected. Therefore Equation (4.3) rewritten as

$$\rho \left[\frac{\partial \vec{u}}{\partial t} + (\vec{u} \cdot \nabla)\vec{u} \right] = -\nabla p + \nabla \tau_{ij} \tag{4.4}$$

Where $\vec{u}$ is velocity vector, p is static pressure and τ_{ij} is the stress tensor and for incompressible it can be written as

$$\tau_{ij} = \mu\left(\nabla\vec{u} + \nabla\vec{u}^{T}\right) \tag{4.5}$$

Therefore governing differential equations are rewritten as

$$\begin{gathered}\nabla\cdot\vec{u} = 0 \\ \rho\left[\frac{\partial\vec{u}}{\partial t} + \left(\vec{u}\cdot\nabla\right)\vec{u}\right] = -\nabla p + \nabla\cdot\left[\mu\left(\nabla\vec{u} + \nabla\vec{u}^{T}\right)\right]\end{gathered} \tag{4.6}$$

4.1 Non-Newtonian Viscosity of Blood

The rheological behavior of blood characterized by a shear rate dependent non-Newtonian viscosity. Blood is classified as shear thinning fluid, which means its viscosity decreases with increased shear rates. Studies [14] have shown that at the shear rates higher than 200 s^{-1} viscosity of blood exhibits Newtonian characteristic and remains constant by approaching an asymptotic value of blood viscosity called infinite shear viscosity, μ_{∞}.

Viscoelastic properties, which make blood non-Newtonian depend on elastic behavior of red blood cells. Blood viscosity increases with increased hematocrit, which is the ratio of the volume of the red blood cells to the total volume of blood. The infinite shear viscosity of blood is 0.00345 Pa·s at hematocrit 33-45%, [14].

In a numerical simulation of blood flow through the vessels, various constitutive equations, which define the relationship between viscosity and shear rate, can be utilized to specify the non-Newtonian viscosity of blood.

4.2 Carreau Model of Blood Viscosity

As the shear rate becomes higher, the viscosity approaches the Newtonian value, μ_∞ which is also called infinite shear viscosity.

Carreau model uses a power-law mathematical expression of blood viscosity written as

$$\mu = \mu_\infty + \frac{\mu_0 - \mu_\infty}{\left[1+\left(\lambda\dot{\gamma}\right)^2\right]^{\frac{1-n}{2}}} \tag{4.7}$$

Where λ is time constant, $\dot{\gamma}$ is the shear rate, n is a coefficient that empirically determined, and μ_0 and μ_∞ are the upper and lower limits of the viscosity corresponding to the low and high shear rates.

4.3 Initial and Boundary Conditions

4.3.1 Case 1: Steady Flow

Average velocities were determined from the flow rates in each vessel using

$$\bar{V} = \frac{Q}{A} \tag{4.8}$$

Where Q is volume flow rate (m^3/s) and A is the surface area (m^2). The average velocities are specified at the inlets of the extended IJVs and SCVs for the first simulation. Later, these vessels are shortened to actual lengths and the velocity profiles at these distances obtained from the first simulation were specified at the IJV and SCV inlets.

Static pressure boundary conditions were specified at the outlets based on the averaged value of measured pressure during a cardiac cycle in the pulmonary arteries, where the average pressure is defined as

$$\bar{P} = \frac{1}{t_c}\int_0^{t_c} P dt \tag{4.9}$$

4.3.2 Case 2: Unsteady Flow

The total pressure is specified at the inlet, and is defined as

$$p_{total} = p + \frac{1}{2}\rho u^2 \tag{4.10}$$

Where p is static pressure, and the second term on the right hand side is the dynamic pressure with ρ density and u velocity. At the outlets, time dependent static pressure tracings, and at the IJV and SCV inlets, constant parabolic velocity profiles throughout the cardiac cyle were applied.

4.4 Numerical Formulation

In this research the FVM was used to discretize the governing differential equations. The FVM is based on the integral form of the conservation equations. It divides the fluid domain into smaller control volumes called cells. Each governing differential equation is integrated over each cell, and fluxes are approximated at the interfaces between adjacent cells. The dependent variables u and p are solved at the each cell's center.

Integrating the continuity equation over a control volume,

$$\int_{V} (\nabla \cdot \vec{u}) dV = 0 \tag{4.11}$$

By applying Gauss Divergence Theorem which is

$$\int_{V} (\nabla \cdot \overline{F}) dV = \int_{A} (\overline{F} \cdot \vec{n}) dA \tag{4.12}$$

Where $\overline{F}$ is a vector quantity and $\vec{n}$ is the unit normal vector to a control surface, A,

Continuity equation (4.2) is written as

$$\int_{A} (\vec{u} \cdot \vec{n}) dA = 0 \tag{4.13}$$

Now, integrating conservation of momentum equation over a control volume,

$$\int_{V} \left[\frac{\partial(\rho \vec{u})}{\partial t} + \vec{u} \nabla \cdot (\rho \vec{u}) \right] dV = \int_{V} \left[-\nabla p \right] dV + \int_{V} \left[\nabla \cdot \left(\mu \left(\nabla \vec{u} + \nabla \vec{u}^{T} \right) \right) \right] dV \tag{4.14}$$

Using Gauss Divergence Theorem,

$$\frac{\partial}{\partial t} \int_{V} (\rho \vec{u}) \, dV + \int_{A} \vec{u} (\rho \vec{u} \cdot \vec{n}) \, dA = \int_{A} -p \cdot \vec{n} \, dA + \int_{A} \left(\mu (\nabla \vec{u} + \nabla \vec{u}^{T}) \right) \cdot \vec{n} \, dA \tag{4.15}$$

Therefore the governing differential equation that are used in FV are

$$\begin{gathered} \int_{A} (\vec{u} \cdot \vec{n}) dA = 0 \\ \frac{\partial}{\partial t} \int_{V} (\rho \vec{u}) \, dV + \int_{A} (\rho \vec{u}) (\vec{u} \cdot \vec{n}) \, dA = \int_{A} -p \vec{n} \, dA + \int_{A} \left(\mu (\nabla \vec{u} + \nabla \vec{u}^{T}) \right) \cdot \vec{n} \, dA \end{gathered} \tag{4.16}$$

4.4.1 Discretization

In order to illustrate discretization of the governing equations easily, the unsteady conservation equation for a transport of a scalar quantity ϕ is written as

$$\int_V \frac{\partial \rho \phi}{\partial t} dV + \int_A \rho \phi \vec{u} \cdot d\vec{A} = \int_A \Gamma_\phi \nabla \phi \cdot d\vec{A} + \int_V S_\phi dV \tag{4.17}$$

Where $\vec{A}$ is surface area vector, Γ_ϕ is diffusion coefficient for ϕ, $\nabla \phi$ is gradient of ϕ, and S_ϕ is the source of ϕ per unit volume.

Equation 4.19 is applied to each control volume, or cell, in the computational domain. In Figure 4.1, a two dimensional triangular cell is shown as an example of CV. Discretization of Equation 4.17 on a given cell is

$$\frac{\partial \rho \phi}{\partial t} V + \sum_f^{N_{faces}} \rho_f \vec{u}_f \phi_f \cdot \vec{A}_f = \sum_f^{N_{faces}} \Gamma_\phi \nabla \phi_f \cdot \vec{A}_f + S_\phi V \tag{4.18}$$

Where N_{faces} is number of faces enclosing cell, ϕ_f is value of ϕ convected through face f, $\rho_f \vec{u}_f \phi_f$ is mass flux through the face, $\vec{A}_f$ is area of face f, $\nabla \phi_f$ is gradient of ϕ at face f, and V is cell volume. First term on the left side of Equation 4.18 is defined in temporal discretization.

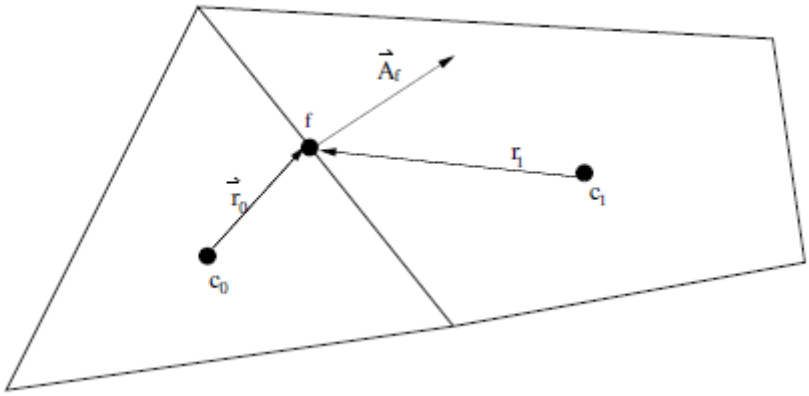

Figure 4.1: CV used to illustrate discretization of a scalar transport equation

The discretized scalar transport equation (4.18) contains the unknown scalar variable ϕ at the cell center as well as the unknown values in surrounding neighboring cells. This equation in general is non-linear with respect to these variables. A linearized form of Equation (4.18) can be written as

$$a_p \phi_p = \sum_{nb} a_{nb} \phi_{nb} + b \tag{4.19}$$

Where the subscript nb refers to neighbor cells, and a_p and a_{nb} are the linearized coefficients for ϕ and ϕ_{nb}.

Similar equations can be written for each cell in the mesh. This results in a set of algebraic equations with a sparse coefficient matrix. For scalar equations Fluent solves this linear system using a point implicit (Gauss-Seidel) linear equation solver.

Fluent stores discrete values of the scalar ϕ at the cell centers. However, face values ϕ_f are required for the convection terms in Equation (4.18) and must be interpolated from the cell center values. This is accomplished using the upwind scheme.

First order upwinding means that the face value ϕ_f is derived from the quantities in the cells upstream relative to the direction of the normal velocity.

Multidimensional linear reconstruction approach is used to compute quantities at cell faces in order to obtain second-order accuracy. In this approach, higher order accuracy is achieved at cell faces through a Taylor series expansion at the cell centered solution about the cell centroid. When second-order upwinding is selected, the face value ϕ_f is computed using the Equation (4.20)

$$\phi_{f,SOU} = \phi + \nabla \phi \cdot \vec{r} \tag{4.20}$$

Where $\vec{r}$ is displament vector from the upstream cell centroid to face centroid. In order to determine $\nabla\phi$ in each cell Fluent offers three methods,

- Green Gauss Cell-Based
- Green Gauss Node-Based
- Least Squares Cell-Based

Gradients are not only needed to evaluate values of a scalar at the cell faces, but also to compute secondary diffusion terms and velocity derivatives.

In this study least squares cell-based method is utilized. This method assumes that the solution varies linearly. The change in cell center values between cell c0 and ci along the vector δr_i from the centroid of the cell c0 to ci is expressed as

$$\left(\nabla\phi\right)_{c0}\cdot\Delta r_i=\left(\phi_{ci}-\phi_{c0}\right) \tag{4.21}$$

When similar equations for each cell surrounding cell c0 are written, the system

$$\left[J\right]\left(\nabla\phi\right)_{c0}=\Delta\phi \tag{4.22}$$

Is obtained. Where J is coefficient matrix, which is a function of geometry.

The spatial discretization for the time dependent equations is identical to the steady state case. Temporal discretization involves the integration every term in the differential equations over a time step Δt.

A generic expression for time evolution of a variable ϕ is given by

$$\frac{\partial\phi}{\partial t}=F(\phi) \tag{4.23}$$

Where the function F incorporates any spatial discretization. For a scalar quantity ϕ using backwards differences second order temporal discretization is given by

$$\frac{3\phi^{n+1} - 4\phi^{n} + \phi^{n-1}}{2\Delta t} = F(\phi) \tag{4.24}$$

Where $n+1$ is value at the next time level, $t + \Delta t$, $n-1$ is value at the previous time level, $t - \Delta t$, and n is value at the current time level, t. Time implicit integration method is used to evaluate F at future time level.

$$\frac{\phi^{n+1} - \phi^{n}}{\Delta t} = F(\phi^{n+1}) \tag{4.25}$$

This is referred to as implicit integration since ϕ^{n+1} in a given cell is related to ϕ^{n+1} in neighboring cells through $F(\phi^{n+1})$:

$$\phi^{n+1} = \phi^{n} + \Delta t F(\phi^{n+1}) \tag{4.26}$$

This implicit equation can besolved iteratively at each time level before moving to the next time step.

4.5 Numerical Solution Technique

4.5.1 Geometric Model

The geometric models were created using Autodesk Inventor software. Case 1 consists of simulations of the BGS in the absence of the mBT shunt. Figure 4.2 and Figure 4.3 show the idealized models used for Case 1 and Case 2, respectively. These models were created in order to develop a computational fluid dynamics model using ANSYS Fluent software.

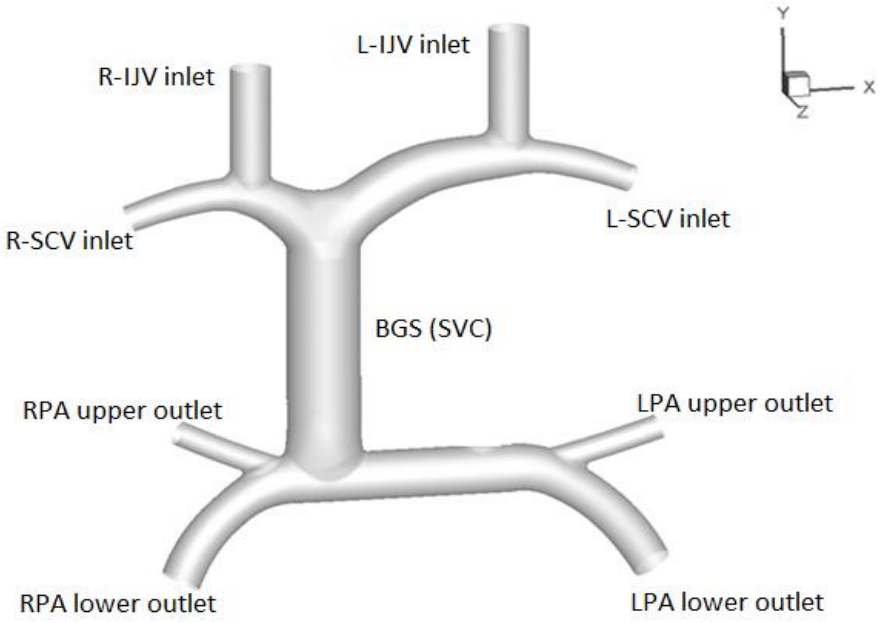

Figure 4.2: Geometry 1 (BGS)

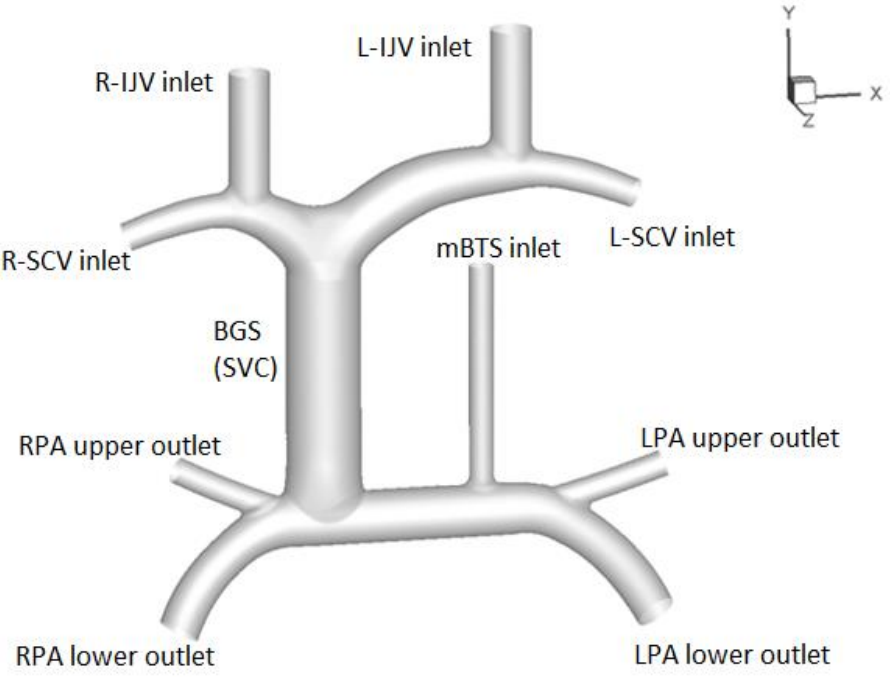

Figure 4.3: Geometry 2 (BGS and mBTS)

4.5.2 Mesh Setup

In order to mesh the geometry, ANSYS Meshing software that allows us to control meshing parameters with variety of user settings was utilized.

Tetrahedral cells were created for the overall domain with a layer of prismatic cells at the vessel walls to predict the high velocity gradients caused by boundary layer more accurately. To create the layer of prismatic cells at the vessel walls, the inflation layer feature of Ansys meshing was used. The inflation layer was specified by its number of layers, the thickness of its first layer, and the growth rate.

For Geometry 1, the number of the mesh elements was 1,537,118 and, for Geometry 2 it was 1,597,653.

Table 4.1 shows the mesh settings that were chosen for this study. The meshed geometry was illustrated in Figure 4.4 and Figure 4.5.

Table 4.1: Mesh settings

Mesh max size	$5x10^{-4}$ mm
First layer thickness of the inflation	$5x10^{-5}$ mm
The number of the inflation layers	9
The growth rate of the inflation layers	1.07
The number of mesh elements	1,537,118 (geometry 1)
	1,597,653 (geometry 2)
The number of mesh nodes	475,092 (geometry 1)
	499,614 (geometry 2)

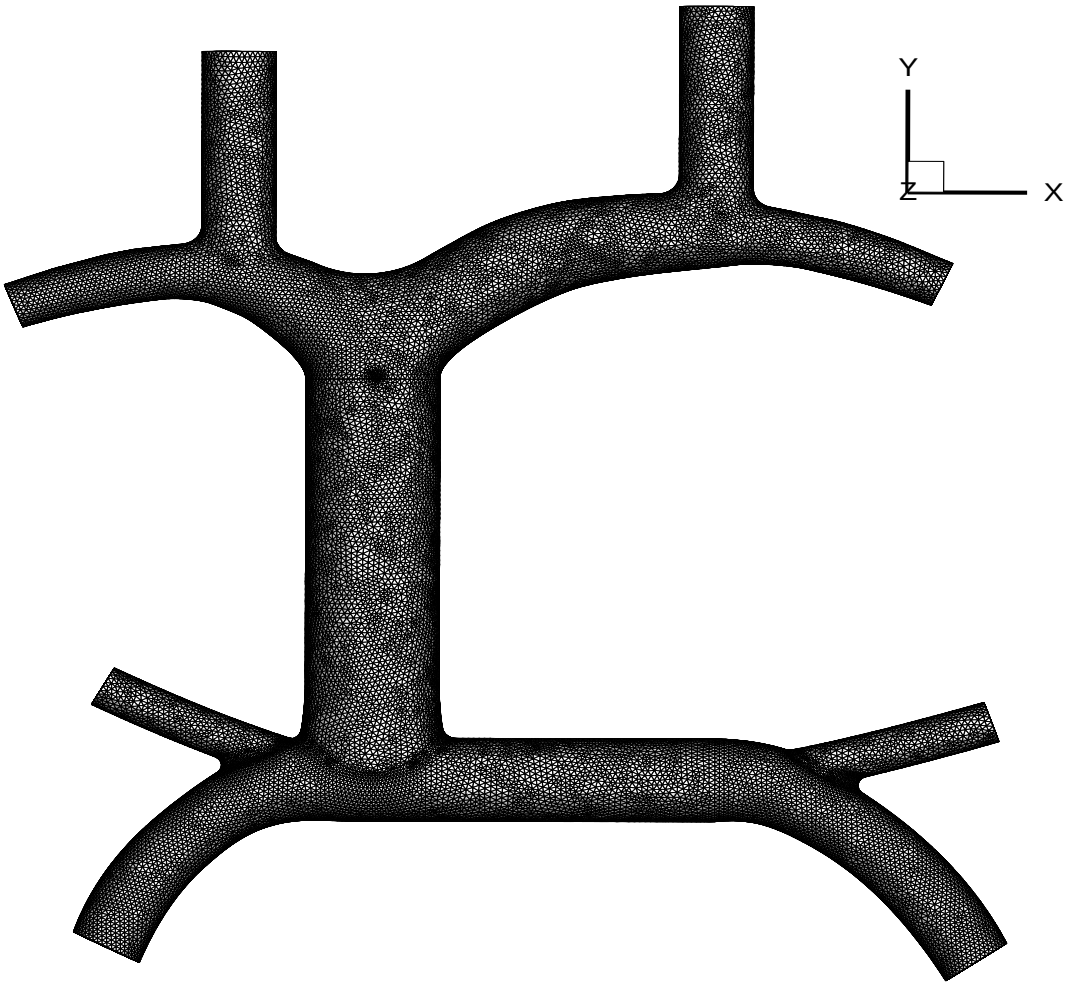

Figure 4.4: Meshed geometry

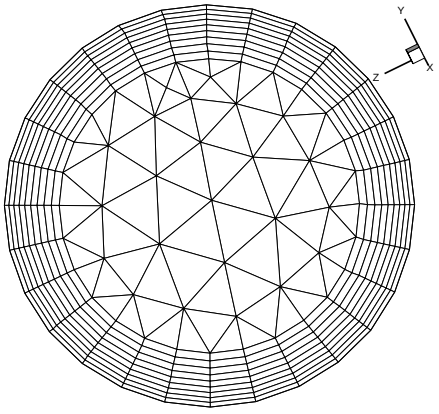

Figure 4.5: Meshed LPA upper outlet

4.5.3 Solution Setup

Fluent offers two kinds of solvers, namely; density based and pressure based, in order to linearize the discretized equations. In density based solver, the continuity equation is used to determine density field. The pressure field is determined from the equation of state. In the pressure based solver, the pressure field is obtained by solving the pressure or pressure correction term, which is found by manipulating the continuity and momentum equations. The density based solvers were designed for high velocity compressible flow. On the other hand, the pressure based solvers were developed for low velocity incompressible flow. However, both approaches are now applicable to a broad range of flows from incompressible to highly compressible. In this study, the pressure based solver was used, since the flow velocity is low and flow was assumed to be incompressible.

There are two kinds of pressure based solver algorithms: the pressure based segregated algorithm and the pressure based coupled algorithm.

The pressure based segregated solver uses a solution algorithm where the pressure correction and momentum equations are solved sequentially. For example using the SIMPLE algorithm introduced by Patankar [19], solves the individual governing differential equations for the solution variables one after another. Each governing equation, while being solved, is "decoupled" from other equations. Since the governing differential equations need to be stored in the memory one at a time segregated solver algorithm does not require very large memory allocation. However, solving the equations in a decoupled manner slows iterative convergence.

The pressure based coupled algorithm solves the degrees of freedom simultaneously. Since the momentum and continuity equations are solved in a closely coupled manner, iterative convergence of the solution significantly improves compared to the segregated algorithm. But the memory requirement increases since the discrete system of all momentum and pressure-based continuity equations needs to be stored in the memory when solving for the velocity and pressure fields. In this study coupled algorithm along with second order upwinding was chosen to perform simulations. The second order upwind scheme uses three data points for spatial accuracy which offers more accurate finite difference stencil than a first order upwinding for the approximation of spatial derivative. It takes into account the flow direction when determining the value at a cell face approximated by a second order upwind extrapolation. It basically, uses the upstream values to evaluate the properties on the cell boundaries and then uses them to compute the value at the cell center. Since it uses a larger stencil and gives a better accuracy, the second order upwinding is chosen for this study.

4.5.4 Fluid Properties

A non-Newtonian Carreau viscosity model with a density of 1060 kg/m^3 was chosen along with the following curve fitting parameters for non-Newtonian Carreau model [14],

$$\lambda = 3.313\ s$$
$$n = 0.3568$$
$$\mu_0 = 0.056 kg/m \cdot s$$
$$\mu_\infty = 0.0345 kg/m \cdot s$$

Where λ is the time constant and n is the power-law index. The shear rate, $\dot{\gamma}$, in Equation (4.7) is the velocity gradient and determined by Ansys Fluent as a part of solution.

4.5.5 Boundary Conditions

Boundary conditions previously described in section 4.3. For the steady state simulations (Case 1) the parabolic inlet velocity profile determined from flow rates were specified at the L-IJV, L-SCV, R-IJV, R-SCV inlets. The averaged velocities at these inlets are 0.138m/s, 0.194 m/s, 0.124 m/s, and 0.168 m/s, respectively. For the outlet boundary conditions the averaged PA pressure of 1599.86 Pa was specified at the LPA upper and lower, and RPA upper and lower outlets. The velocity at the walls is zero.

For the unsteady simulations (Case 2), the mBTS that supplies pulsatile flow from the aorta was added to Geometry 1. The measured time dependent aortic pressure tracing was specified as inlet boundary condition at the mBTS inlet. At the L-IJV, L-SCV, R-IJV, R-SCV inlets and the walls, the same boundary conditions specified for Case 1 were applied. At the LPA upper and lower, and RPA upper and lower outlets the measured time dependent PA pressure tracing was specified. Figure 4.6 shows the time dependent aortic and PA pressure traces that were used at the mBTS inlet and outlets for the unsteady simulations.

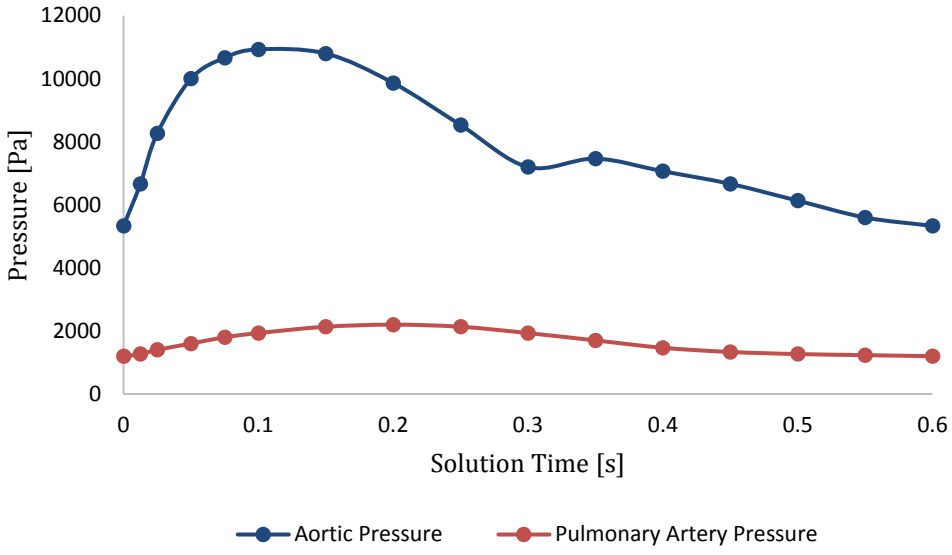

Figure 4.6: Aortic and Pulmonary Artery Pressure Traces for the unsteady case

5 Results

5.1 Mesh Independence Study

The results of any CFD analysis must be independent from the mesh that is used in the simulations to obtain them. Before computing the results of this study, a mesh independence study was conducted to determine mesh requirements for a converged solution. In this study the simulations were run for six different meshes by changing the number of inflation layers and maximum mesh size. The growth rate of the inflation feature was held fixed.

The results for the following parameters are used to justify the mesh chosen (mesh 2) for the remainder of study and they are presented in Table 5.1, Table 5.2, Table 5.3, and Table 5.4 with the percent differences.

- Maximum wall shear stress
- Static pressure at the L-IJV inlet
- Kinetic energy at the LPA upper outlet
- Total pressure at the LPA upper outlet

Table 5.1 shows the maximum wall shear stresses that are determined using six different meshes with the percent differences from mesh 2. Static pressures at the L-IJV inlet that are computed using the same meshes are indicated in Table 5.2. At the L-IJV inlet velocity boundary condition is applied. Therefore, static pressure is chosen to compare for each number of mesh elements. At the LPA outlet, the static pressure boundary condition is applied. In table 5.3 and 5.4, respectively the kinetic energies and

total pressures are shown with the percent differences from mesh 2 that are computed using different number of mesh elements.

Table 5.1: Maximum wall shear stresses and percent differences in results using different meshes

	Number of mesh elements	Max wall shear stress (Pa)	Percent difference compare to the mesh chosen
1	674,431	5.5	1.3
2	1,537,118	5.4	0
3	2,005,584	5.4	0.1
4	2,732,215	5.4	0.2
5	3,012,366	5.4	0.2
6	3,213,692	5.4	0.3

Table 5.2: Static pressure at the L-IJV inlet and percent differences in results using different meshes

	Number of mesh elements	Static pressure at the L-IJV inlet (Pa)	Percent difference compare to the mesh chosen
1	674,431	1671.5	0.022
2	1,537,118	1671.1	0
3	2,005,584	1671.2	0.005
4	2,732,215	1671.2	0.003
5	3,012,366	1671.3	0.010
6	3,213,692	1671.1	0.001

Table 5.3: Kinetic energy at the LPA upper outlet and percent differences in results using different meshes

	Number of mesh elements	Kinetic energy at the LPA upper outlet (Pa)	Percent difference compare to the mesh chosen
1	674,431	11.5	1.058
2	1,537,118	11.6	0
3	2,005,584	11.6	0.114
4	2,732,215	11.6	0.002
5	3,012,366	11.6	0.247
6	3,213,692	11.6	0.010

Table 5.4: Total pressure at the outlet and percent differences in results using different meshes

	Number of mesh elements	Total pressure at the LPA upper outlet (Pa)	Percent difference compare to the mesh chosen
1	674,431	1611.3	0.007
2	1,537,118	1611.5	0
3	2,005,584	1611.5	0.000
4	2,732,215	1611.5	0.000
5	3,012,366	1611.5	0.001
6	3,213,692	1611.5	0.000

Figure 5.1 shows the percent differences of maximum wall shear stress, static pressure at the L-IJV inlet, and total pressure and kinetic energy at the LPA outlet from mesh 2. As the number of mesh elements increases, the percent differences from mesh 2 remains under one percent. Therefore, the results will be independent from the mesh chosen for the remainder of the study.

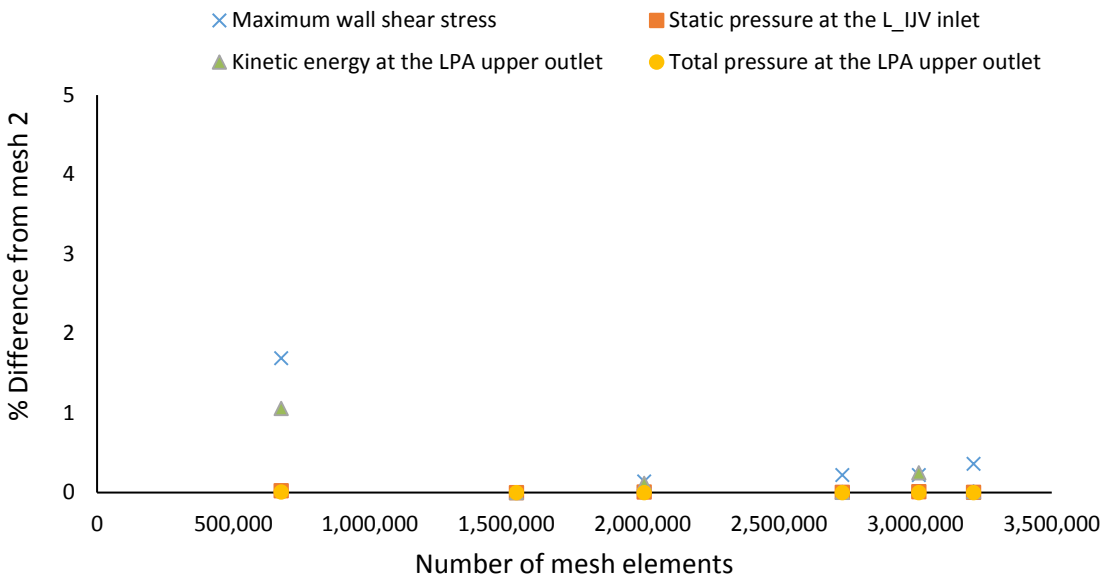

Figure 5.1: The number of mesh elements and percent differences from mesh 2

5.2 Time Independence Study

In the second case of this study, the time dependent measured aortic pressure tracing was specified at the mBTS inlet; and the measured pulsatile pulmonary artery pressure tracing was specified at the LPA upper and lower, and RPA upper and lower outlets. At the L-IJV, L-SCV, L-IJV, and R-IJV inlets of the domain, the parabolic velocity profile was specified.

The time independence study was conducted in order to ensure that the results are independent from the time step size used in the simulations. The unsteady simulations were run for geometry 2 and for 5 cardiac cycles using a time step size of $1.2x10^{-2}$ s, $6x10^{-3}$ s, and $3x10^{-3}$ s. The results of each simulation for the last cardiac cycle were written every two time steps.

The results were used to justify the time step size of 0.006 used for the remainder of study and presented in Table 5.5. Wall shear stress, volume flow rate at the mBTS inlet, static pressure at the L-IJV inlet, and total pressure at the LPA outlet are averaged over a cardiac cycle. The boundary conditions applied are total pressure tracing, parabolic velocity profile, and static pressure tracing at the mBTS inlet, L-IJV inlet, and LPA outlet, respectively. The simulations with different time steps were run for five cardiac cycles and the results of the last cardiac cycles are monitored. Figure 5.2 indicates the percent differences from the results that were obtained from the last cardiac cycle using a time step size of $6x10^{-3}$. The percent differences between results obtained using the time step sizes of 0.006 and 0.003 are smaller than one percent. Therefore, the results are independent from the time step size used for the remainder of this study.

Table 5.5: The results of the pulsatile simulations run for different time step size

Time step size	$1.2x10^{-2}$	$6x10^{-3}$	$3x10^{-3}$
Average wall shear stress (Pa)	9.3	9.1	9.1
Volume flow rate at the mBTS inlet (L/min)	1.8	1.8	1.8
Static pressure at the L-IJV inlet (Pa)	1941.0	1944.3	1937.9
Total pressure at the LPA upper outlet (Pa)	1744.6	1740.6	1757.7

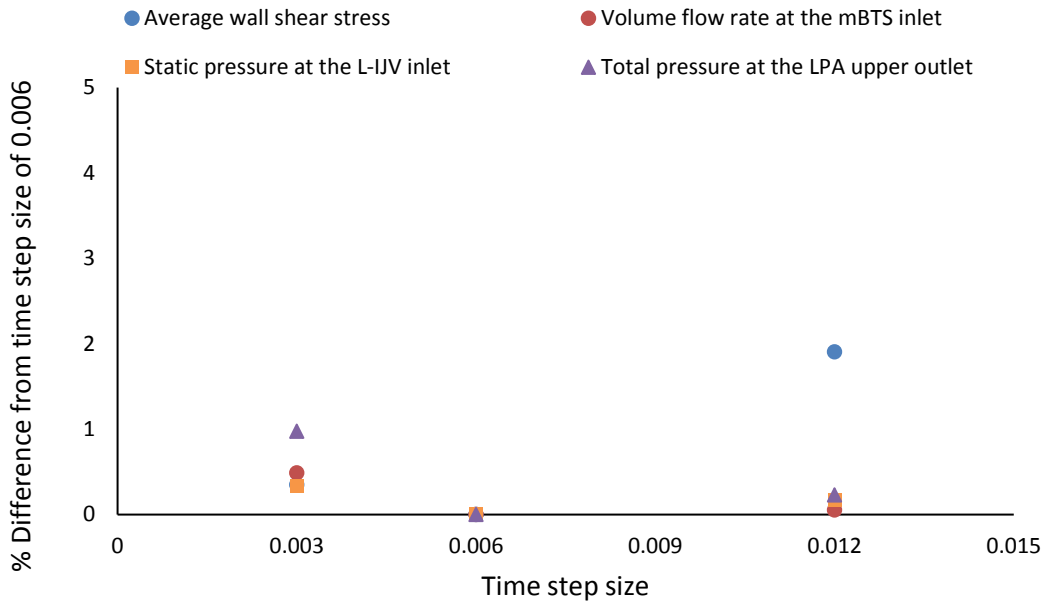

Figure 5.2: Percent differences of results from the time step size of 0.006

5.3 Case 1: Steady Flow Results

In this section, the results of steady simulations using Geometry 1 are presented using first Newtonian viscosity of 0.00345 Pa·s and then non-Newtonian viscosity as previously described in section 4.5.4. Inlet and outlet boundary conditions were specified at the domain boundaries as described in section 4.5.5.

The wall shear stress contour plot results for Case 1 using Newtonian and non-Newtonian viscosity models are given in Figure 5.3 and Figure 5.4, respectively. The wall shear stress distributions on the walls of Geometry 1 are almost identical in the Newtonian and non-Newtonian case. The wall shear stress increases at the vascular connections where the R-IJV and R-SCV, and L-IJV and L-SCV are, respectively connected to the R-INV and L-INV (green-yellow regions in Figure 5.3 and Figure 5.4), and bifurcations where LPA and RPA flows separates to the upper and lower branches (yellow-red regions in Figure 5.3 and Figure 5.4) for both Newtonian and non-

Newtonian case. It also slightly increases where the blood flow from INVs merges at the inlet of the BGS and when blood flow from the BGS separates to LPA and RPA (light blue regions in Figure 5.3 and 5.4). Table 5.6 indicates the results of average BGS wall shear stress, average PA wall shear stress, average pressure in the BGS, total energy loss, flow energy efficiency, percentage of the flow rate to the RPA, and percentage of the flow rate to the LPA that were obtained using Newtonian and non-Newtonian blood viscosity with percent differences. Differences in average pressure and velocity in the BGS, energy efficiency, and percentage of the flow rates to the LPA and RPA are less than two percent. However, compared to these results, the absolute percent differences in total energy loss and average BGS and PA wall shear stresses are high, respectively, 9.4 %, 10.7 % and 12.1 % between the Newtonian and non-Newtonian case. Since there are such differences in total energy loss and average wall shear stress, the Newtonian simulations took as long as non-Newtonian simulations, and the non-Newtonian model is a more realistic description of blood rheology, it was decided to use non-Newtonian blood viscosity model for the remainder of the simulations.

Wall shear stress magnitude obtained using non-Newtonian Carreau viscosity model varies between 0 and 5.73 Pa as it is shown in Figure 5.4. It increases due to sudden changes in flow direction at the vascular connections. The shear rate computed for the viscosity of 0.00345 $Pa \cdot s^{-1}$ and the maximum wall shear stress magnitude of 5.73 Pa is 1660 s^{-1}, which is very low compared to the shear rate of 10,500 s^{-1} that initiate platelet activation.

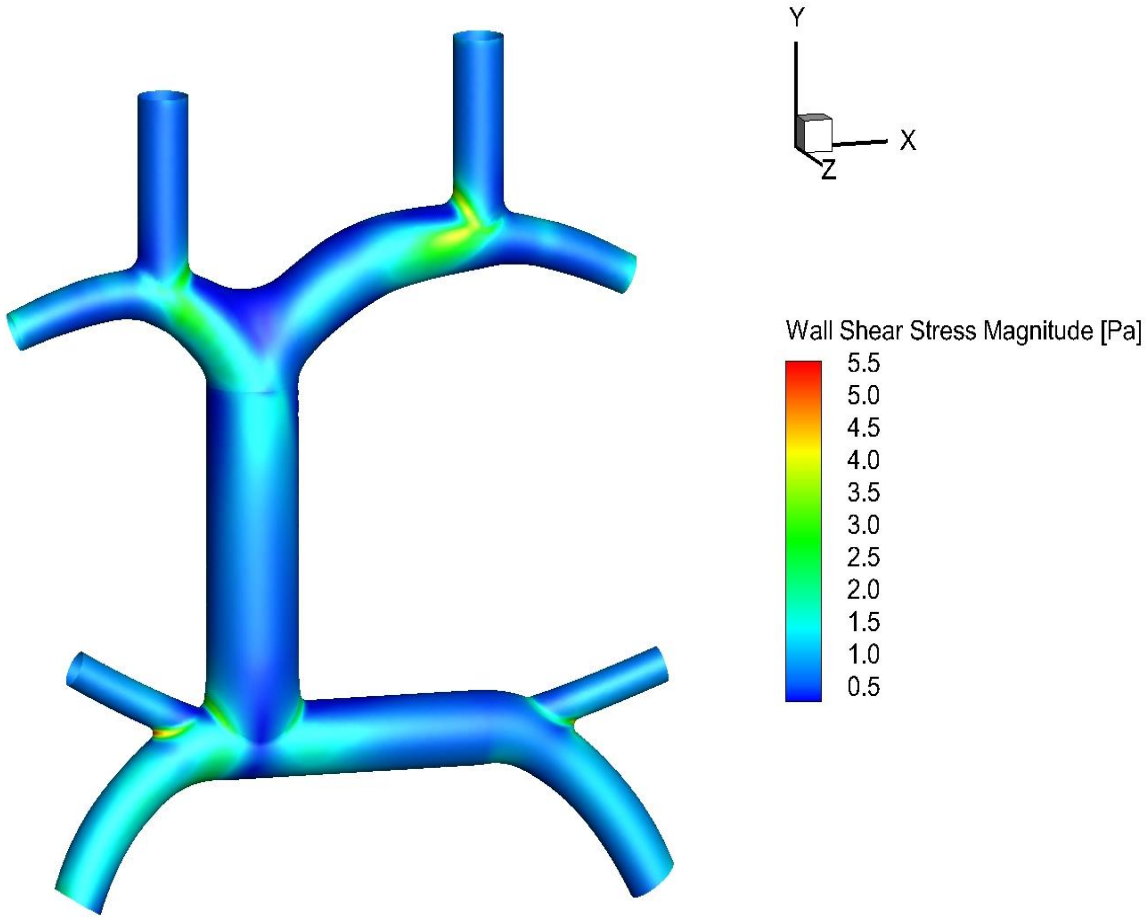

Figure 5.3: Contour plot of wall shear stress magnitude for Case 1 using Newtonian viscosity of μ=0.00345 Pa·s

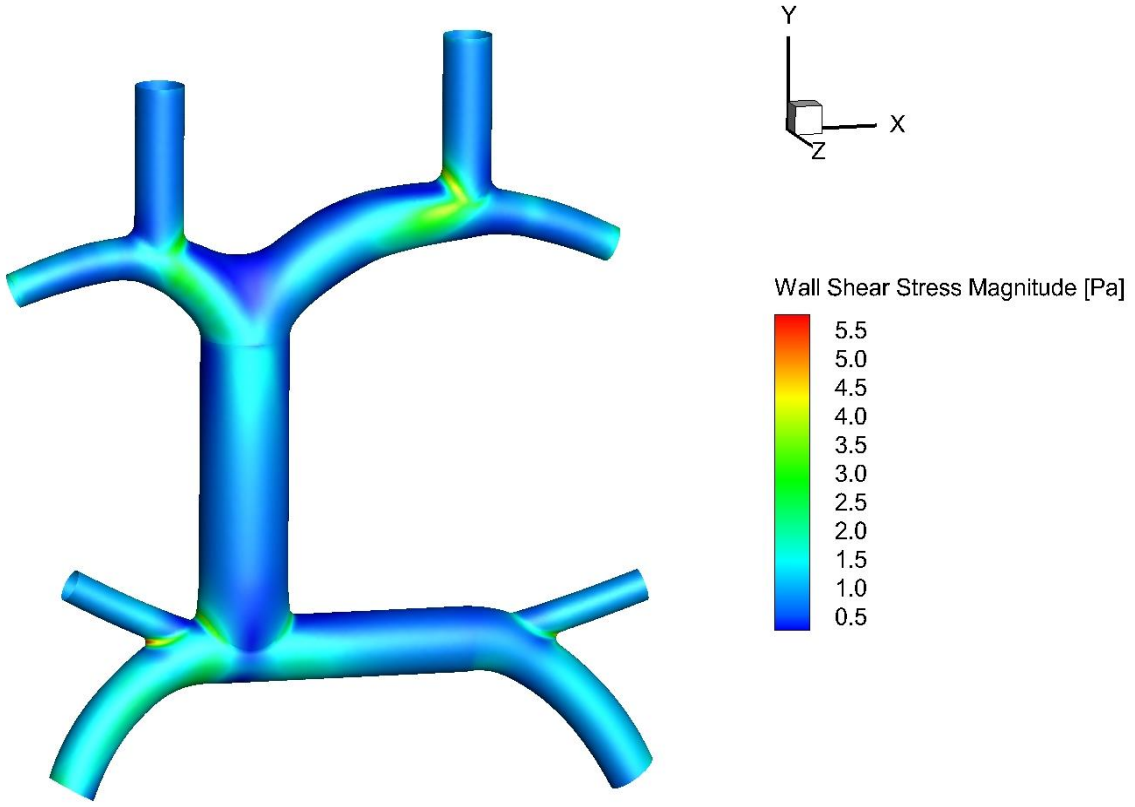

Figure 5.4: Contour plot of wall shear stress magnitude for Case 1 using non-Newtonian Carreau viscosity model

Table 5.6: Comparison of results obtained using Newtonian viscosity of 0.00345 Pa·s and Carreau viscosity model for Case 1.

Viscosity Model	Newtonian	Carreau	Absolute Percent Difference
Averaged BGS wall shear stress (Pa)	0.625	0.700	10.7
Averaged PA wall shear stress (Pa)	0.836	0.952	12.1
Averaged Pressure in the BGS (Pa)	1634.291	1638.020	0.2
Averaged Velocity in the BGS (m/s)	0.137	0.135	1.4
Total energy loss (J/m^3)	60.928	67.311	9.4
% Energy efficiency	96	96	0
% flow rate to the RPA	55.340	54.999	0.6
% flow rate to the LPA	44.660	45.001	0.7

Figure 5.5 shows the pressure contours throughout Geometry 1. Pressure changes between 1600 and 1680 Pa, consistent with the LPA and RPA branch pressures of 1600 Pa. It is highest at the L-IJV and R-IJV inlets, 1670 Pa. In the L-IJV, L-SCV, R-IJV, and R-SCV it changes between 1660 and 1675 Pa. Then it decreases when the blood flow through these vessels merges in the L-INV and R-INV (green-yellow regions where IJVs and SCVs connect to the INVs). It keeps decreasing in the BGS to the average pressure of 1638 Pa. In the LPA and RPA, pressure varies between 1635 and 1620 Pa. In the PA branches, it varies between 1625 Pa and 1600 Pa. Pressure is lowest at the outlets, 1600 Pa.

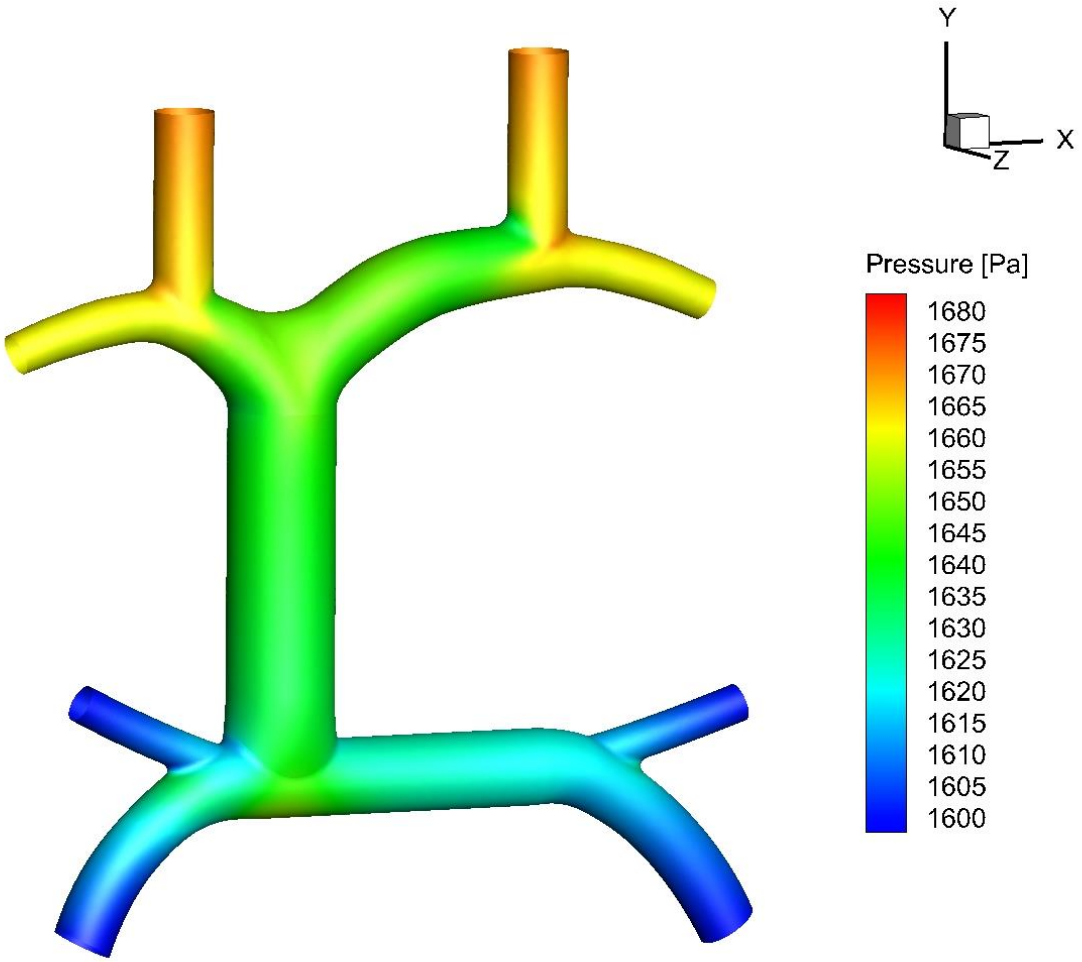

Figure 5.5: Pressure contours for Case 1

Figure 5.6 shows the contour plot of velocity magnitude in the symmetry plane of Geometry 1. Streaming of the flow was directed by the relative position of the veins that drain blood flow to the BGS. Velocity magnitude changes between 0 and 0.35 m/s in the entire domain. It is highest at the L-SCV inlet. When the blood flows through the SCV and IJV merge, velocity increases in the INV (yellow-red region in the INVs). The blood flows though the BGS with an average velocity of 0.135 m/s and the volume flow rate of 1 L/min. In the LPA and RPA, velocity is still low, changes between 0 and 0.18 m/s. It is slightly higher in the RPA lower branch than other branches of PAs.

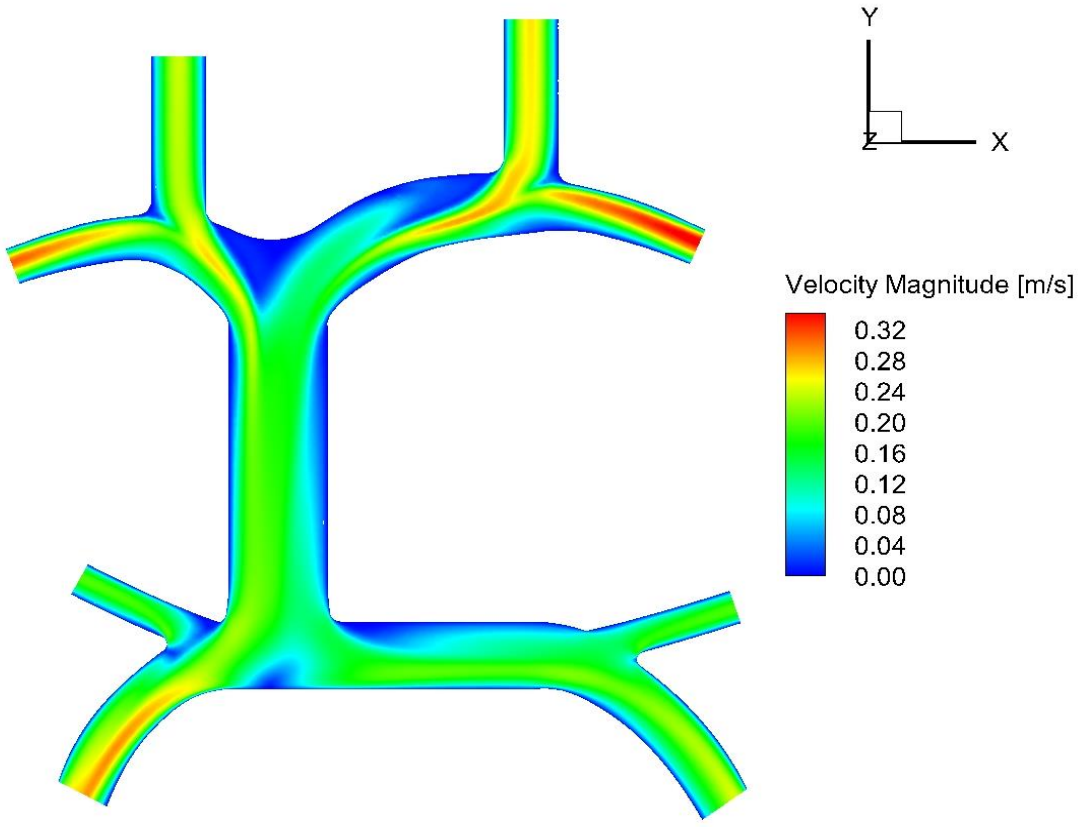

Figure 5.6: Velocity magnitude in the symmetry plane of Geometry 1

Figure 5.7 shows the contour and vector plots of the velocity magnitude at the axis of the BGS. The velocity magnitude in the BGS is low, ranges from 0 to 0.2 m/s. Low velocity blood flow through the BGS creates small vortices at the anterior and posterior walls of the RPA.

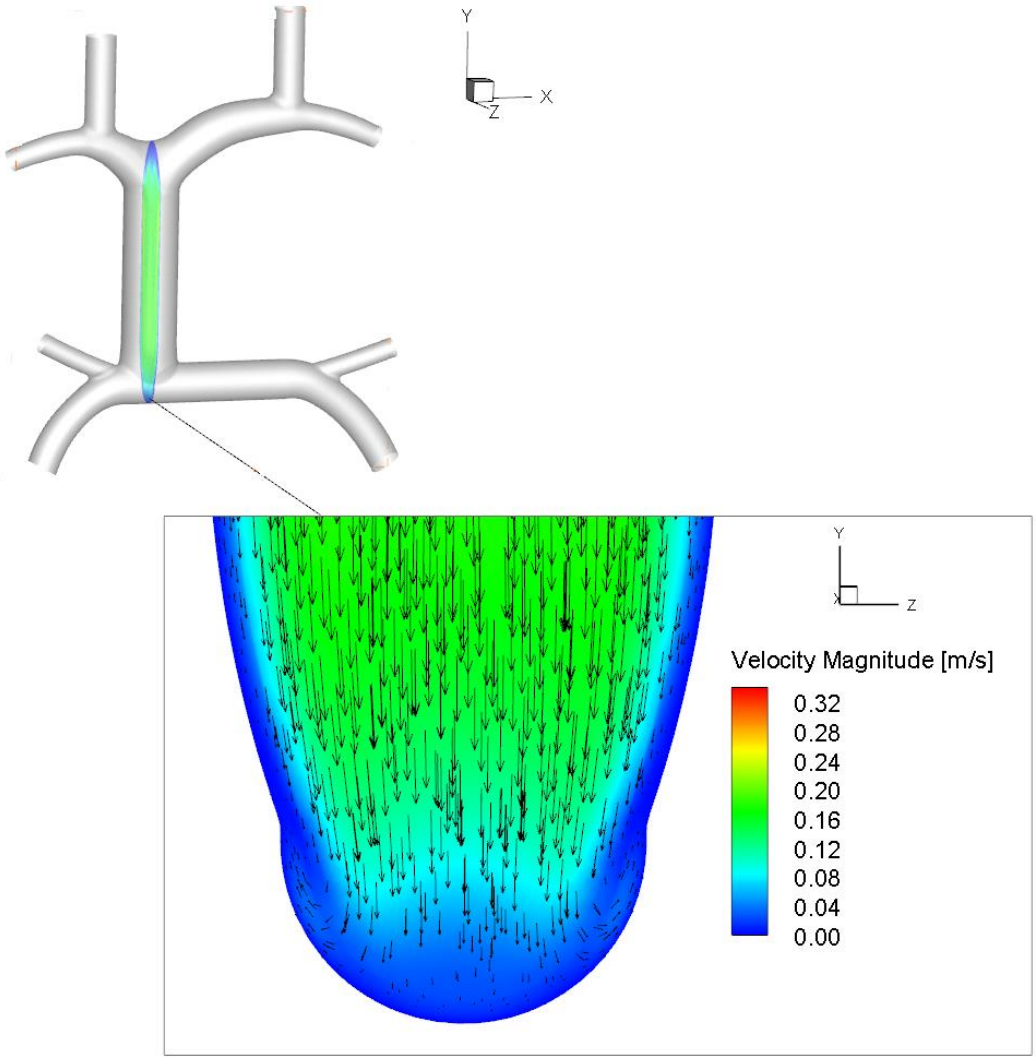

Figure 5.7: Contour and vector plots of velocity magnitude at the axis of BGS for Case 1

Flow rate in the BGS is 1 L/min and 55% (0.55 L/min) and 45% (0.45 L/min) of the incoming flow through the BGS is driven to RPA and LPA, respectively. Since the BGS is the right side, more flow is directed to RPA.

Total energy loss and the energy efficiency of the system were calculated using the equations in Appendix 2 which applies conservation of energy to a control volume. Static pressure, total pressure, and kinetic energy for the inlets and outlets to be used in energy loss calculations were given in Table 5.7.

Table 5.7: Pressure and kinetic energy results for Case 1

	Static Pressure (Pa)	Total Pressure (Pa)	Kinetic Energy (Pa)
L-IJV inlet	1671.02	1690.06	19.04
L-SCV inlet	1661.41	1696.32	34.91
R-IJV inlet	1671.40	1686.97	15.56
R-SCV inlet	1661.21	1687.97	26.75
LPA upper outlet	1599.86	1611.48	11.62
LPA lower outlet	1599.86	1619.20	19.34
RPA upper outlet	1599.86	1611.68	11.82
RPA lower outlet	1599.86	1631.11	31.25

The incoming and outgoing flow energies are computed as 1690.1 J/m^3 (0.027 W) and 1622.8 j/m^3 (0.026 W), respectively. 67.31 J/m^3 (0.01 W), which is 4% of the incoming energy, is lost in Geometry 1. The power efficiency of the system is 96%.

5.4 Case 2: Unsteady Flow Results

In this section, the results of pulsatile simulation using Geometry 2 were presented using non-Newtonian Carreau viscosity model. Inlet and outlet boundary conditions were specified as described in section 4.5.5.

A cardiac cycle refers to a complete heartbeat and includes systole and diastole phases. In systole phase, the heart muscle contracts and pumps the blood into the aorta. Therefore, pressure at the mBTS inlet is highest at systole. Diastole is the phase when heart muscle relaxes and at this phase the aortic pressure is the lowest. In evaluating the pulsatile results, the systole, diastole and the average values over the cardiac cycle were considered.

Wall shear stress at a point on the LPA wall where the mBTS impinges therefore wall shear stress is maximum at peak systole was detected and wall shear stress at this point throughout the cardiac cycle is shown in Figure 5.8. The wall shear stress is maximum at peak systole and minimum at end diastole. The instantaneous wall shear stress distribution at peak systole (0.1 second) and end diastole (0.6 second) is shown in Figure 5.9 and Figure 5.10, respectively. Near the mBTS inlet wall shear stresses are artificially high because of boundary condition approximation. Where the total pressure boundary condition is applied at the inlet, Fluent assumes a uniform velocity profile at the inlet creating a developed region. Further away from the inlet, wall shear is calculated correctly. Wall shear stress is maximum; 280 Pa at the LPA wall where the blood flow exiting the mBTS impinges on the LPA wall and is turned 90˚; producing a region of accelerating flow. The accelerating flow produces a region of high wall shear stress. It decreases as the blood flows through RPA and LPA. Wall shear stress changes

from 280 Pa to 20 Pa and from 160Pa to 8 Pa on the PA walls between the mBTS and BGS at peak systole and end diastole, respectively. The average PA wall shear stress excluding branches was found 44.4 Pa and 20.9 Pa at peak systole and end diastole, respectively. The averaged wall shear stress over the BGS wall is 0.8 Pa at 0.1 second, 0.76 Pa at 0.6 second, and 0.78 Pa when it is averaged over the cardiac cycle. Similarly, averaged wall shear stress over the mBTS wall is 37.3 Pa at 0.1 second, 21 Pa at 0.6 second, and 28.4 Pa when it is averaged over the cardiac cycle.

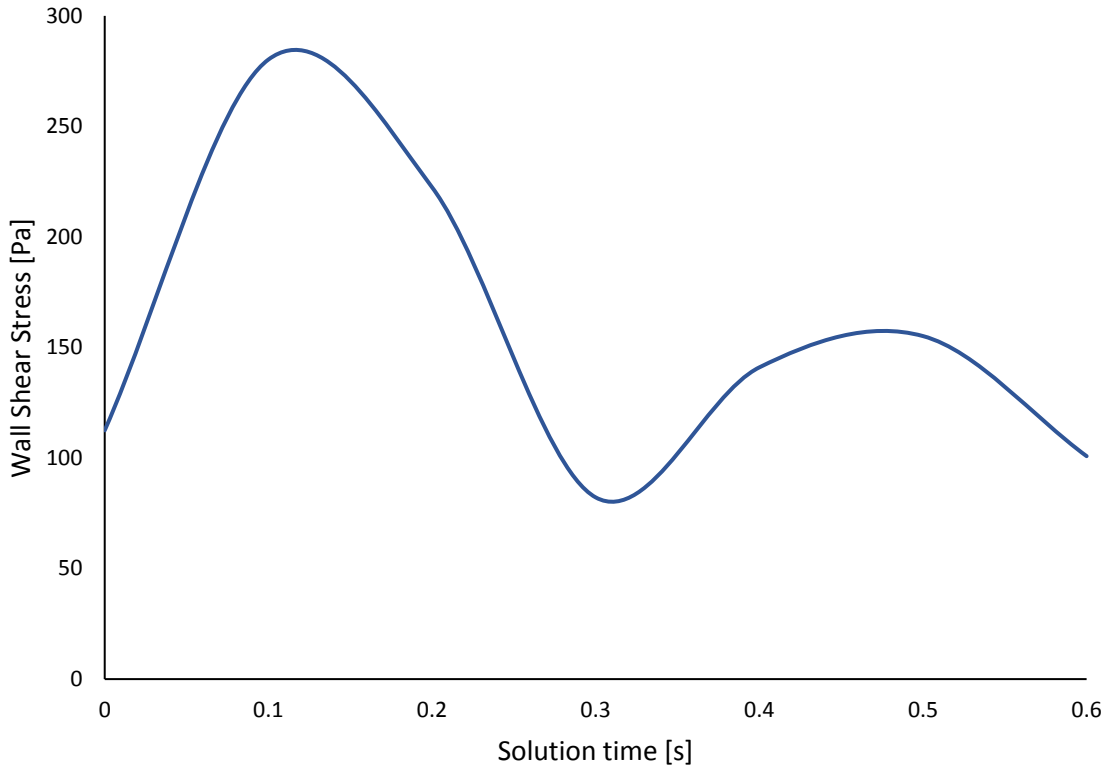

Figure 5.8: Instantaneous wall shear stress magnitude of a point on the LPA wall where the wall shear stress is the highest at peak systole throughout the cardiac cycle. 0.1 second is peak systole and 0.6 second is end diastole.

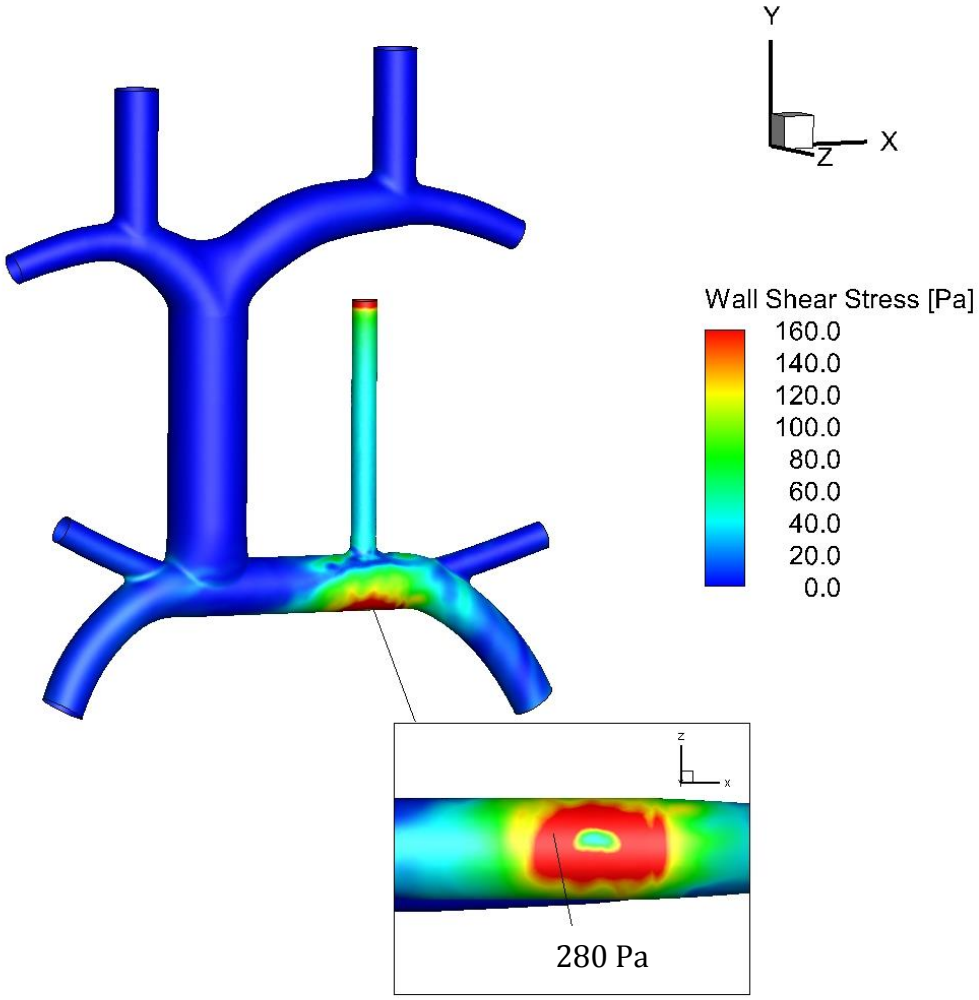

Figure 5.9: Contour plot of wall shear stress magnitude at the time of maximum wall shear stress (peak systole)

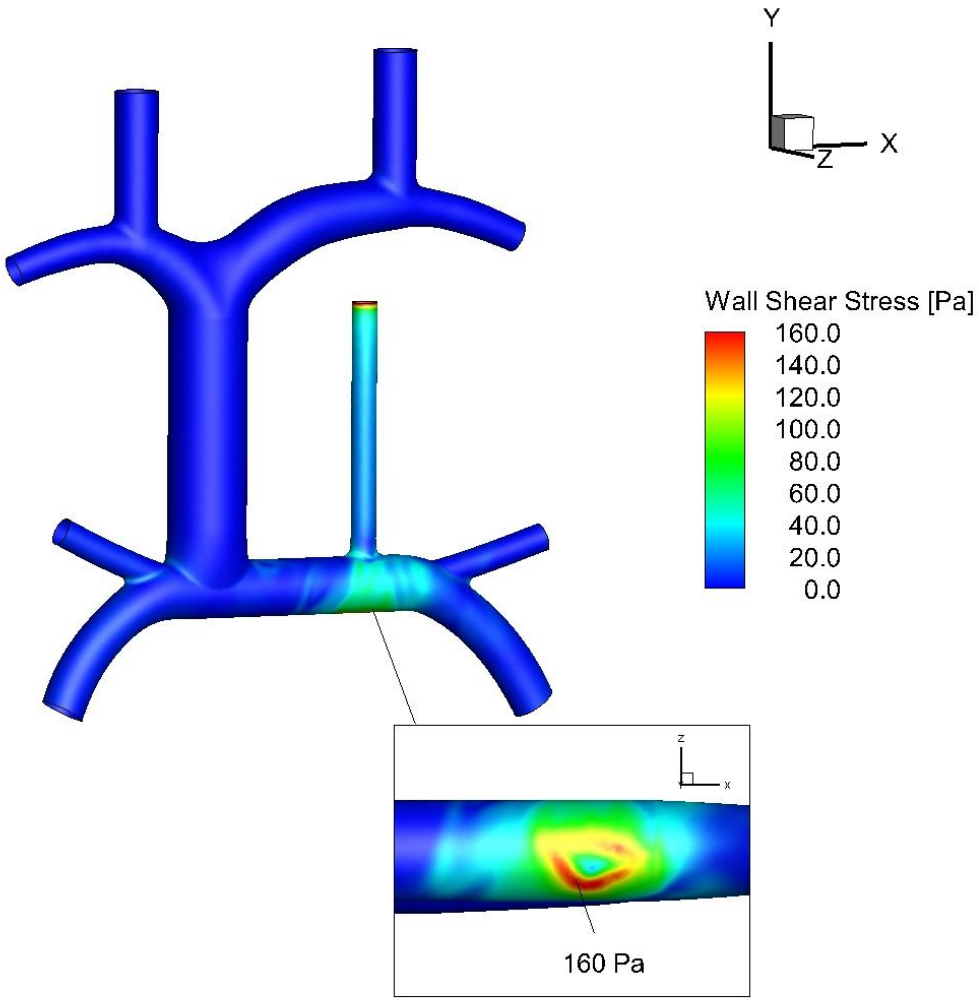

Figure 5.10: Contour plot of wall shear stress magnitude at the time of minimum wall shear stress (end diastole)

The shear rate that initiates platelet activation is 10,500 s^{-1}. The shear rates at the time of maximum and minimum wall shear stress are computed as 75,362 s^{-1} and 46,376 s^{-1} respectively. The shear rates on the PA walls at peak systole and end diastole are high enough to increase platelet activation and cause thrombus formation.

A point on the LPA wall where the mBTS impinges therefore pressure is maximum at peak systole was detected and pressure distributon at this point throughout the cardiac cycle is shown in Figure 5.11. At peak systole, 0.1 second, pressure is highest and at end diastole, 0.6 second, it is lowest. The instantaneous pressure distribution at peak systole and end diastole is shown in Figure 5.12 and Figure 5.13, respectively. Pressure changes from 1600 Pa to 11000 Pa and from 1600 Pa to 5400 Pa throughout Geometry 2 at peak systole and diastole, respectively. It is highest where the mBTS flow strikes the LPA wall. The averaged pressure in the BGS is 2191 Pa at peak systole, 1367 Pa at end diastole, and 1910 Pa when it is averaged over the cardiac cycle. Comparing the pressure results in the BGS for Case 1 and Case 2 (averaging over the cardiac cycle) it is observed that the addition of mBTS increases the average pressure in the BGS from 1638 Pa to 1910 Pa.

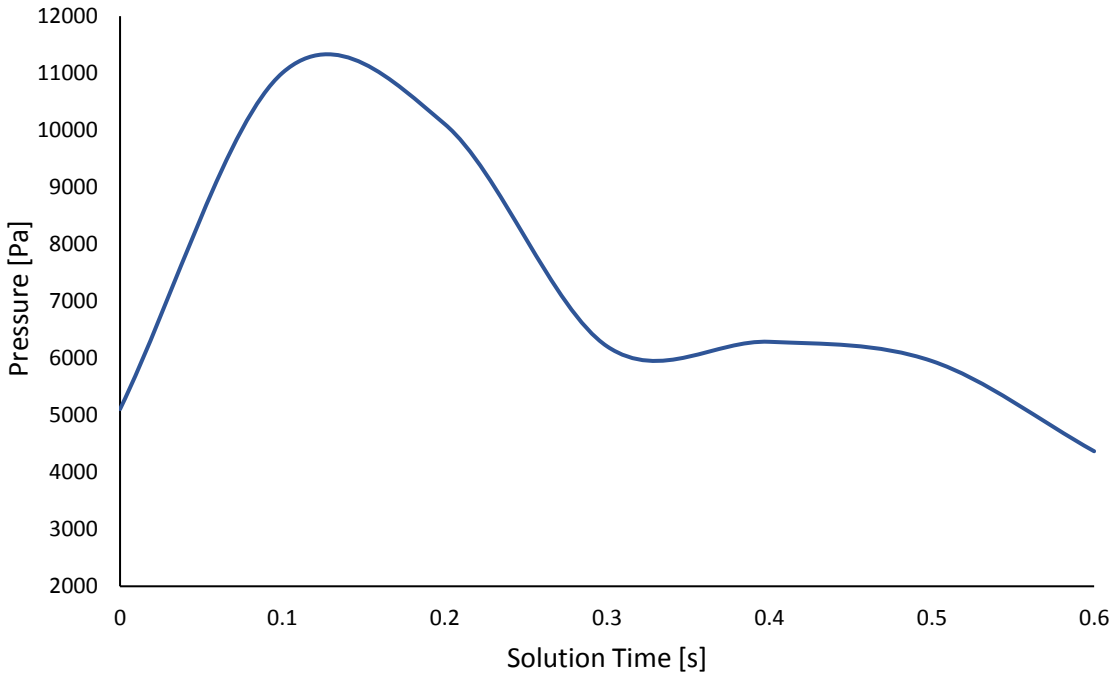

Figure 5.11: Instantaneous pressure of a selected point on the LPA wall where the pressure is the highest at peak systole throughout the cardiac cycle. 0.1 second is the time of maximum and 0.6 second is the time of minimum pressure.

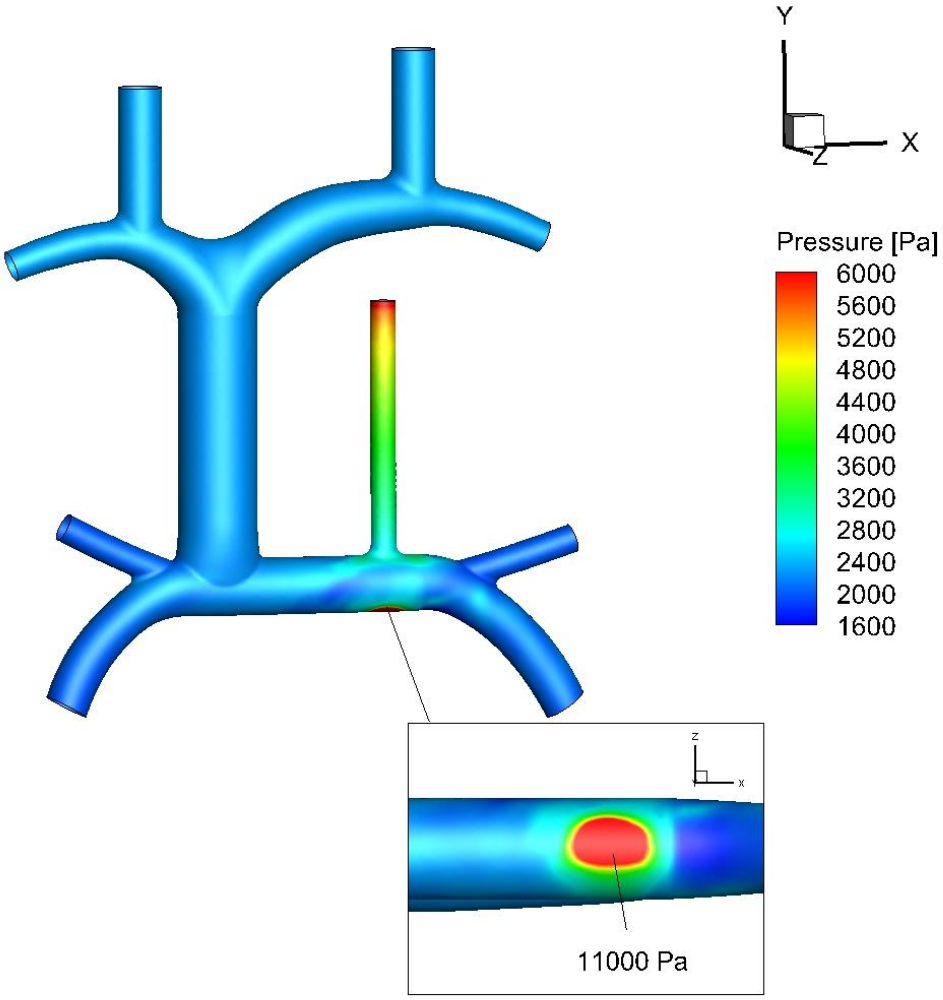

Figure 5.12: Contour plot of pressure at peak systole

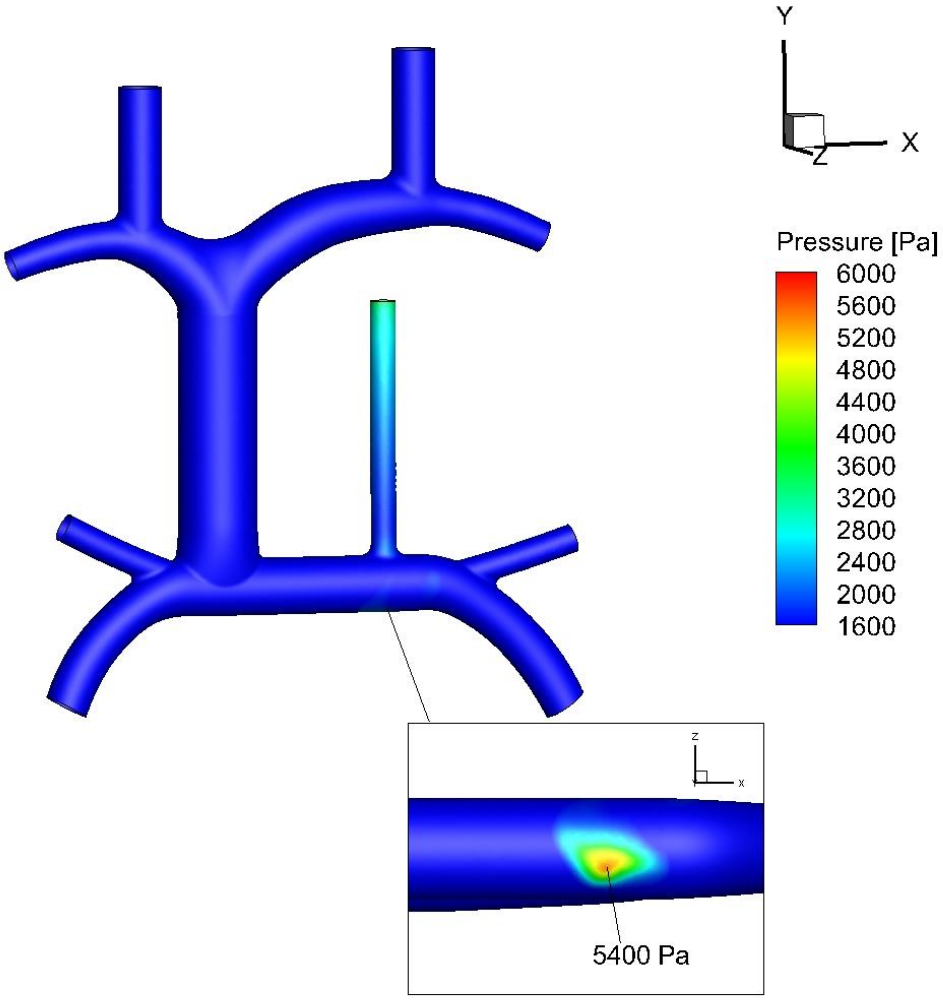

Figure 5.13: Contour plot of pressure at end diastole

A point in the LPA where the mBTS impinges therefore velocity magnitude is maximum at peak systole was detected and velocity magnitude at this point throughout the cardiac cycle is shown in Figure 5.14. The instantaneous velocity magnitude in the symmetry plane of Geometry 2 at peak systole and diastole were shown in Figure 5.15 and Figure 5.16, respectively. At peak systole and diastole, the velocity throughout Geometry 2 changes between 0 and 4 m/s; and 0 to 2.5 m/s, respectively. In the mBTS, velocity is highest. As the flow separates to the LPA and RPA velocity decreases significantly in a small region. This causes high velocity gradients in the PAs. Velocity is very low in the IJVs, SCVs, INVs, and BGS changes from 0 to 0.7 m/s. Similarly, the velocity magnitudes at peak systole and diastole at the axis of the BGS and mBTS are shown in Figure 5.17 and Figure 5.18, respectively. At peak systole and diastole, the average velocities in the BGS were 0.138 m/s and 0.135 m/s, and in the mBTS were 3.013 and 1.931, respectively. The Figures 5.17 and 5.18 indicate that the high velocity pulsatile flow from the mBTS enters the LPA and strikes the LPA wall thereby creating vortices at anterior and posterior walls. These vortices increase the wall shear stress on the LPA wall. As fluid propagates from the LPA to the RPA, the velocity and wall shear stresses decrease. At the axis of the BGS, the flow streamline is disturbed by the flow advancing from the LPA as it is seen in Figure 5.17 and Figure 5.18.

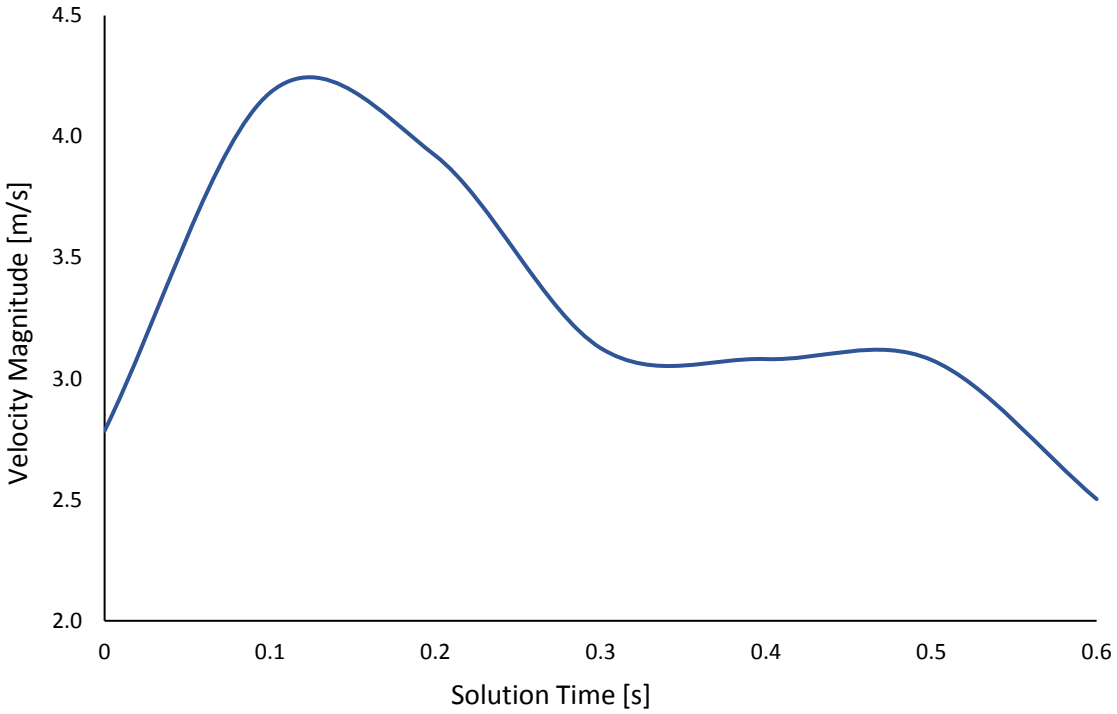

Figure 5.14: Instantaneous velocity magnitude of a selected point in the LPA where the velocity magnitude is the highest at peak systole throughout the cardiac cycle. 0.1 second is the time of maximum and 0 second is the time of minimum velocity magnitude.

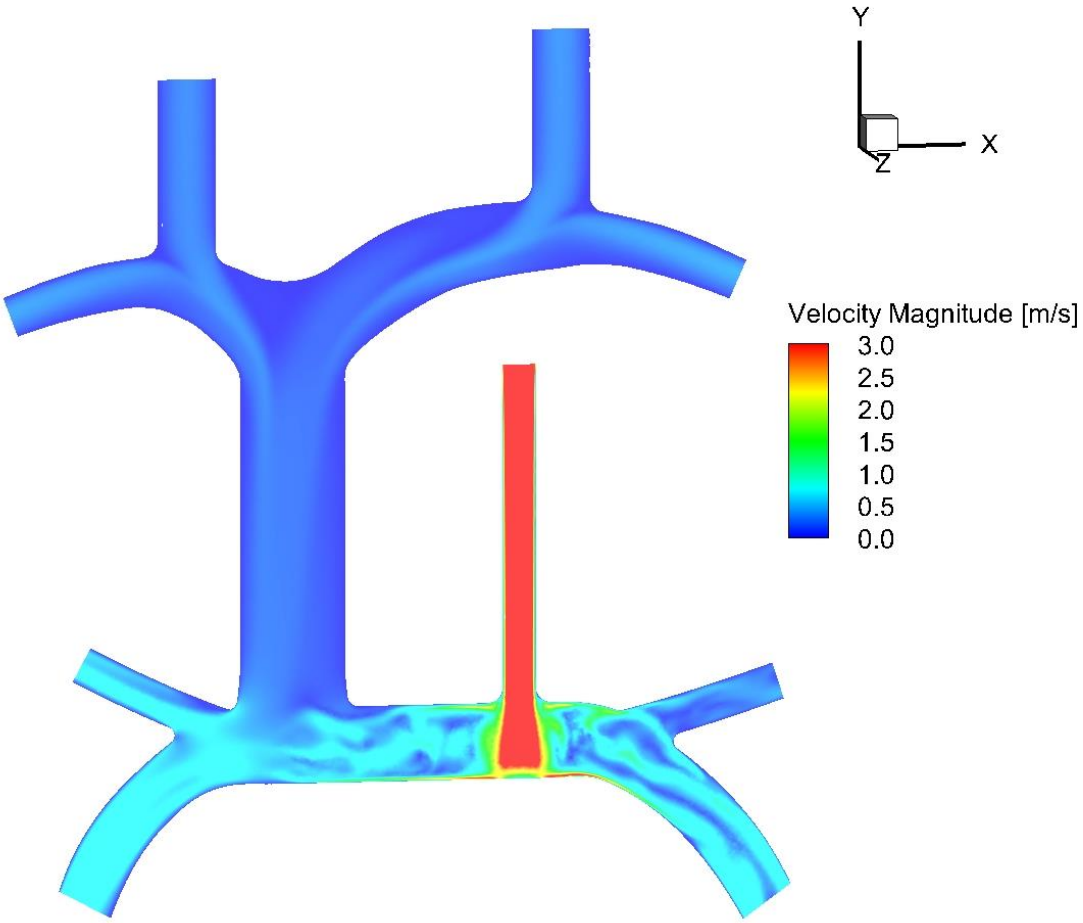

Figure 5.15: Contour plot of velocity magnitude in the symmetry plane of Geometry 2 at the time of maximum velocity magnitude

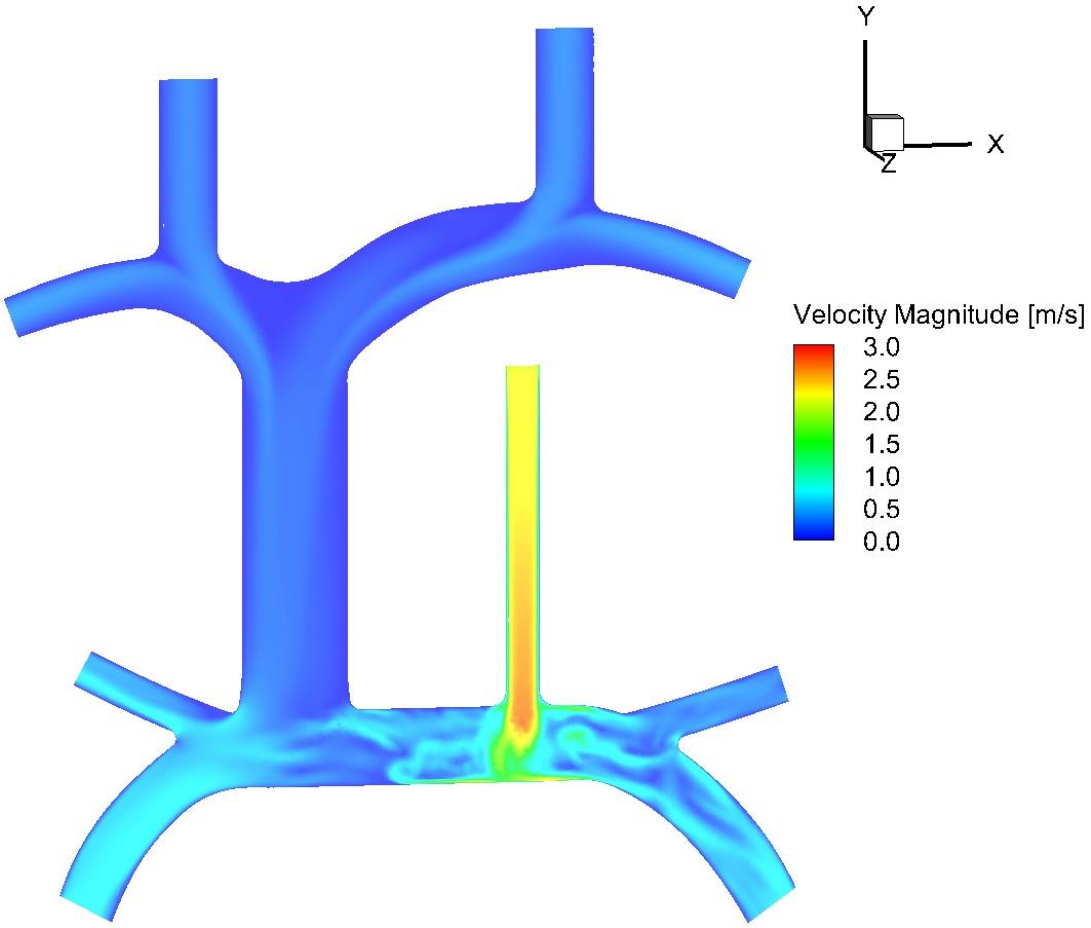

Figure 5.16: Contour plot of velocity magnitude in the symmetry plane of Geometry 2 at the time of minimum velocity magnitude

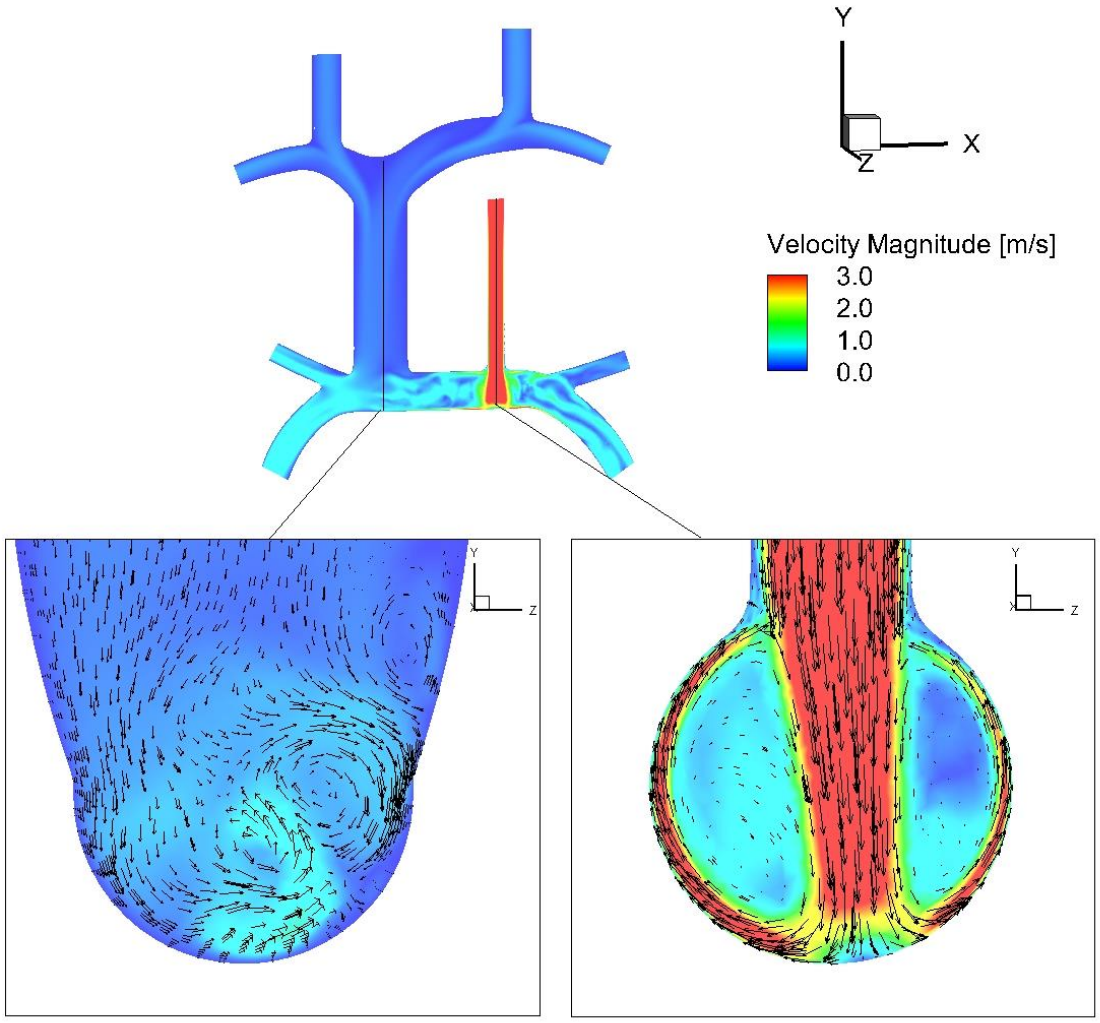

Figure 5.17: Contour plot of velocity magnitude at the axis of BGS and at the axis of mBTS at the time of maximum velocity

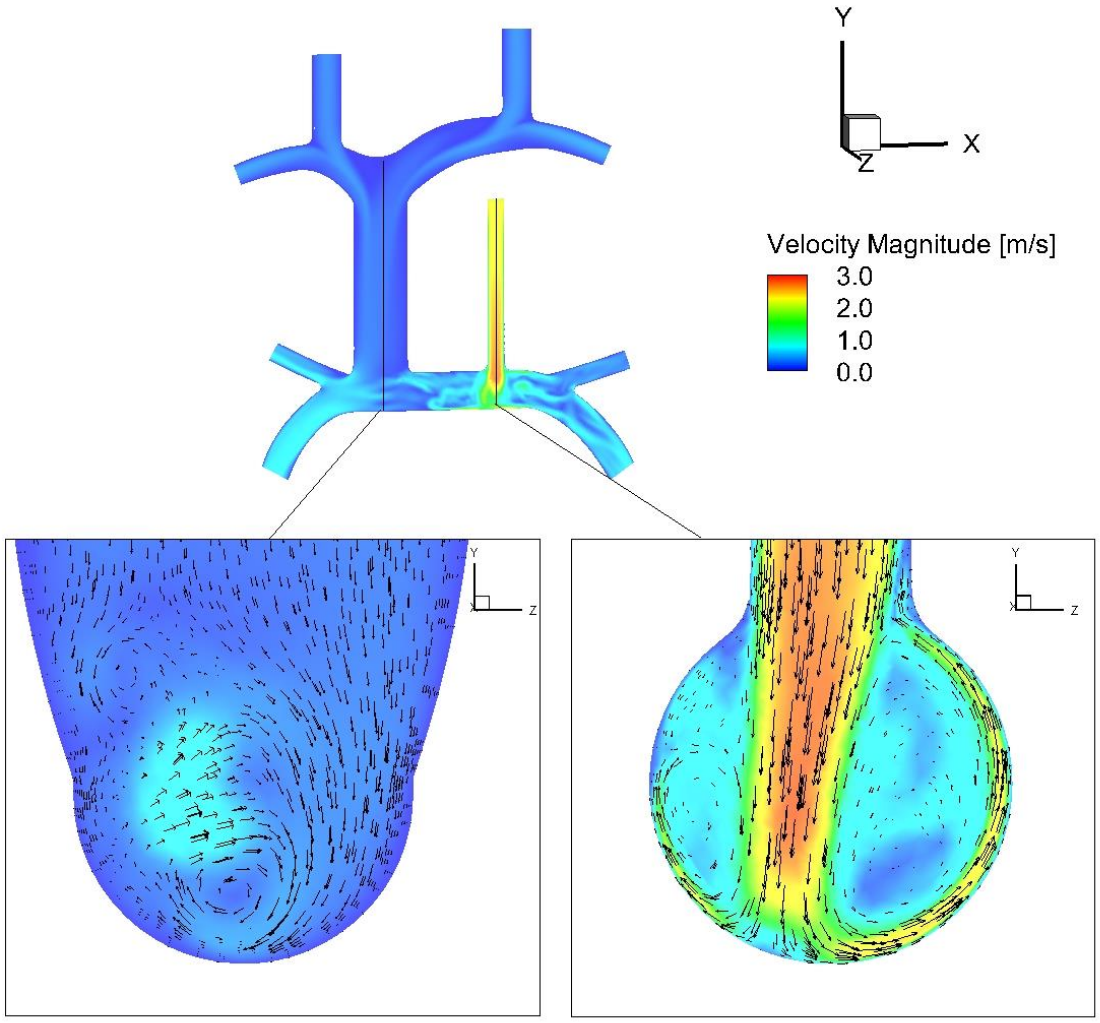

Figure 5.18: Contour plot of velocity magnitude at the axis of BGS and at the axis of mBTS at the time of minimum velocity

Figure 5.19 shows the average wall shear stress magnitude over the cardiac cycle. The geometry is divided between the LPA and RPA and it is illustrated using two different scales for each PA in order to compare the wall shear stress distributions between Case 1 and Case 2. In Case 2, the average wall shear stresses increased to 0.8 Pa on the BGS wall and 30.4 Pa on the PA walls. On the LPA wall, the average maximum wall shear stress over the cardiac cycle is 195 Pa. In Case 1, it was 9.1 Pa.

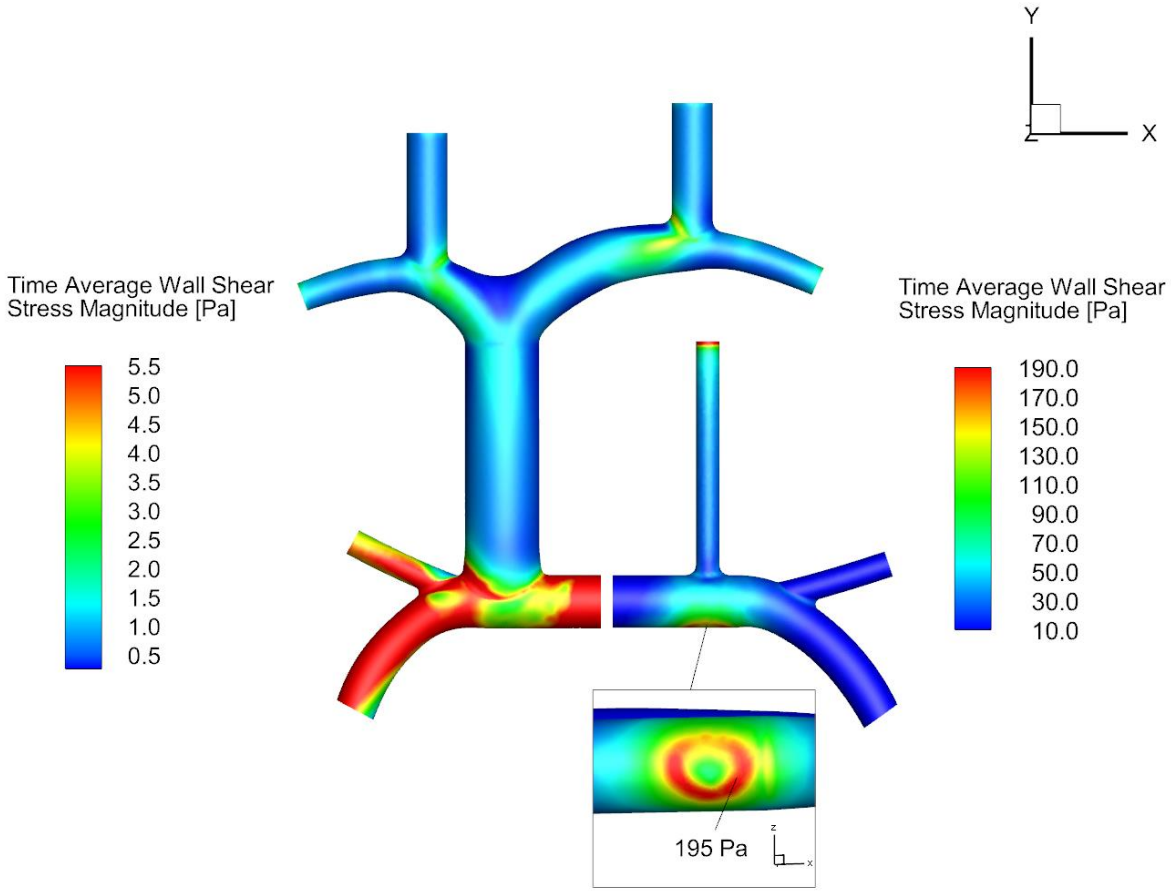

Figure 5.19: Contour plot of time average wall shear stress magnitude under pulsatile flow conditions

Average flow rates through BGS and mBTS are 1 L/min and 1.83 L/min respectively. Forty-five percent and the fifty-five percent of the average incoming flow is driven to the LPA and RPA, respectively. Figure 5.20 indicates the volumetric flow rates through each shunt and PA in Case 2. The results of volumetric flow rates in Case 1 and Case 2 are compared in Table 5.8.

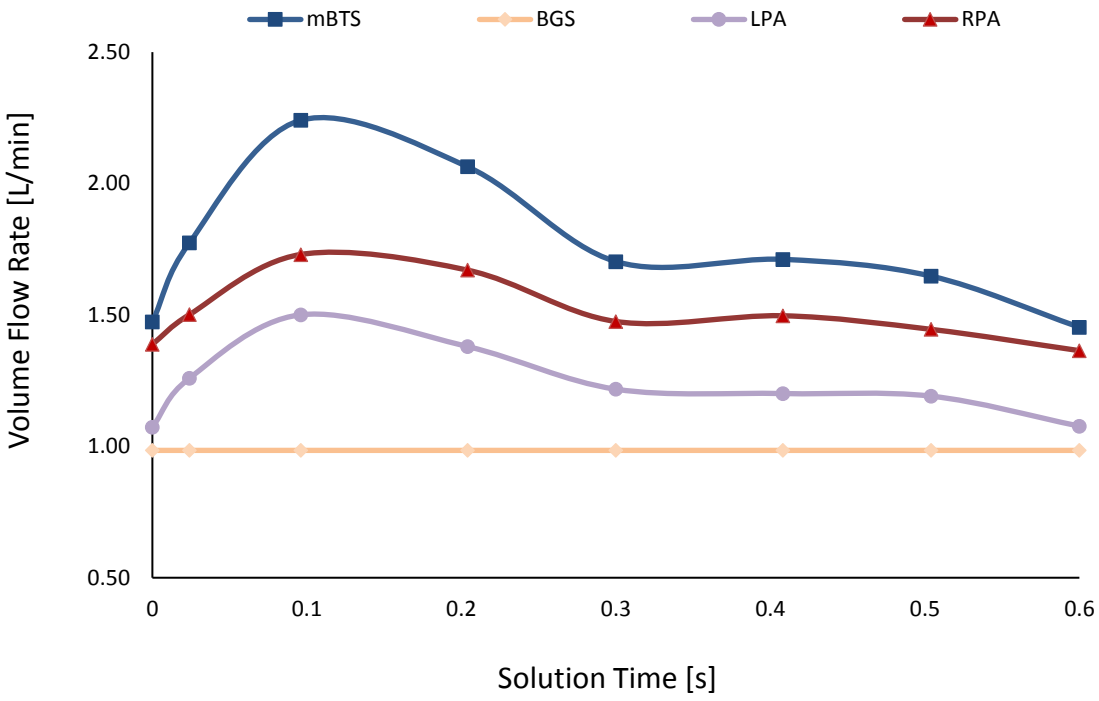

Figure 5.20: Volumetric flow rates through the mBTS, BGS, LPA, and RPA under pulsatile flow conditions

Table 5.8: Volumetric flow rates through BGS, LPA, RPA, and mBTS for Case 1 and Case 2. Unsteady flow rates are averaged over the cardiac cycle.

	Case 1	Case 2
	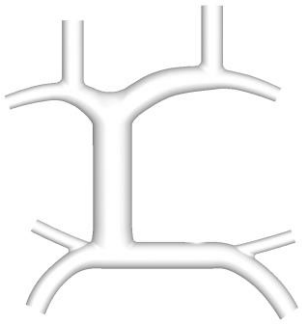	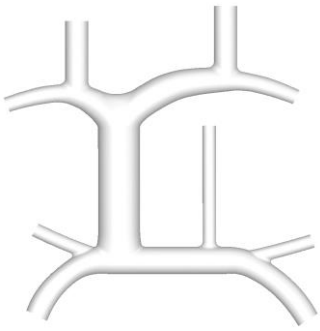
	Flow rates [l/min]	Flow rates [l/min]
BGS	1	1
LPA	0.45	1.28
RPA	0.55	1.55
mBTS	-	1.83

The addition of mBTS increases the flow rates in the LPA and RPA from 0.45 L/min and 0.55 L/min to 1.28 L/min and 1.55 L/min, respectively. This additional pulsatile blood flow from the mBTS to the PAs provides a sufficient PA growth.

Critical Reynolds number is calculated for a non-Newtonian fluid using the Equation (5.1) [20],

$$Re_{cr} = \frac{6464n}{(3n+1)^2}(2+n)^{(2+n)/(1+n)} \tag{5.1}$$

Where n is the index number of non-Newtonian fluid. Therefore, Re_{cr} is computed as 2385.

In both case one and case two, Reynolds number is calculated at the inlets using Equation (5.2) [21],

$$Re = \frac{\rho \bar{V} D}{\mu} \tag{5.2}$$

Where ρ is density (1060 kg/m^3), $\bar{V}$ is averaged velocity, D is diameter of vessel, and μ is viscosity. At each inlet, Re number is calculated substituting μ_0 and μ_∞ for μ. Therefore, the range that Re changes can be compared with Re_{cr}. Table 5.9 shows the range of Re calculated at each inlet. Flow is proved to be laminar at the L-IJV, L-SCV, R-IJV, and R-SCV inlets. However, at the mBTS inlet, Re calculated using the highest averaged velocity at this inlet througout the cardiac cycle which is encountered at peak systole (0.1 second) is 3689.9. Velocities are high only in the mBTS. In this study, the main region of interest includes the BGS and PAs where the velocities are reasonably low to assume that the flow is laminar.

Table 5.9: Reynolds Number calculated using zero and infinite shear viscosity

	Reynolds Number	
	μ_0	μ_∞
L-IJV inlet	17.8	290.4
L-SCV inlet	17.3	281.5
R-IJV inlet	16.0	260.7
R-SCV inlet	15.1	245.4
mBTS inlet	224.1	3686.9

The power loss and power efficiency of the system were computed using the equations in Appendix 2. Figure 5.21 shows the power loss throughout the cardiac cycle. The maximum and minimum power losses are observed at 0.1 second and at 0.6 second, respectively.

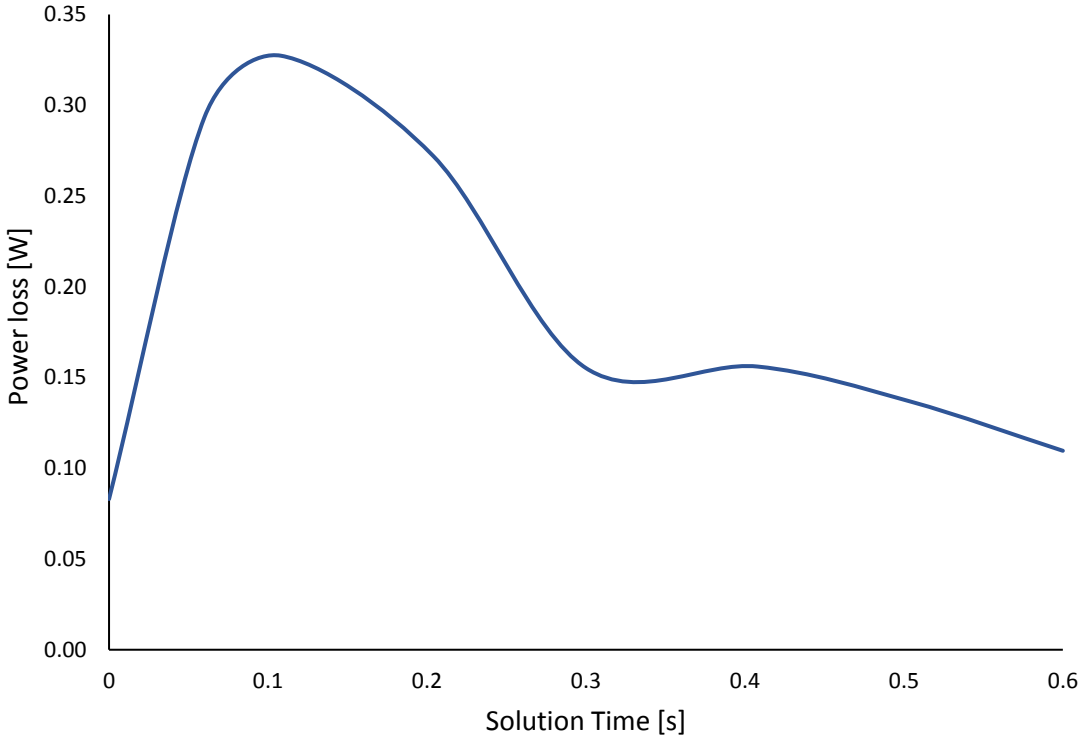

Figure 5.21: The power loss for Case 2 throughout the cardiac cycle

The incoming average power through both the mBTS and the BGS inlet is 0.28 Watts. The power loss is averaged over the cardiac cycle for Case 2 and it is 0.19 Watts. Power efficiency of the system is 31% and the total power that is supplied to the lungs from both the LPA and RPA branch outlets is 0.08 W.

The power loss throughout the cardiac cycle in the PAs excluding branches is shown in Figure5.22. The average power loss over the cardiac cycle in the PAs excluding the branches is 0.18 Watts. The total power loss in the system is 67 percent of the incoming power and 64 percent of the incoming power was dissipated in the PAs. The high gradient of the wall shear stress on the PA walls and the flow interaction between the BGS and mBTS cause the most of the incoming power to dissipate in this region.

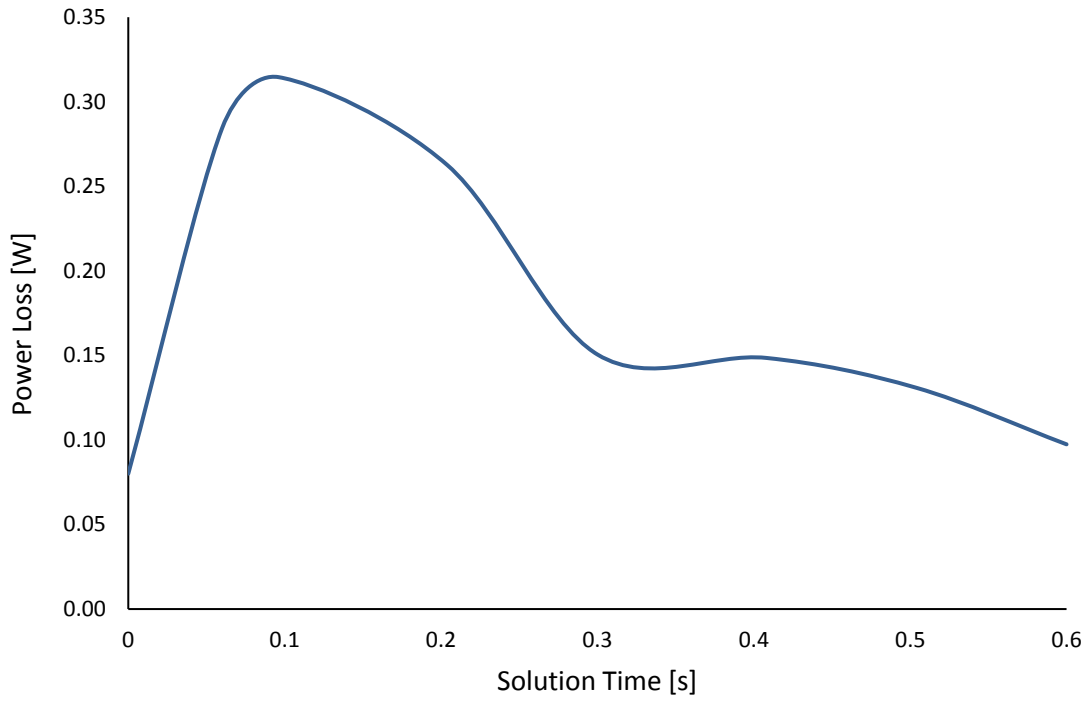

Figure 5.22: The power loss throughout the cardiac cycle in the PAs excluding the branches for Case 2

The energy loss in Case 1 is 67 J/m^3 (2x10^{-4} W) and very small compare to power loss in Case 2, which is 0.19 Watts. The BGS alone is more efficient than the BGS with mBTS. However, the outgoing power that is supplied to the lungs is effectively higher when the BGS is supplemented with the mBTS. The total outgoing power at the PA branch outlets are 1x10^{-3} and 8x10^{-2} W in Case 1 (BGS alone) and Case 2 (BGS and mBTS), respectively.

6 Conclusions

In this research, the effects of having an additional pulsatile blood flow from the mBTS to the PAs on the energy losses and thrombus formation were investigated utilizing CFD. Two cases were studied: in Case 1, steady flow through the BGS is the only source of PA flow, in Case 2, the pulsatile mBTS flow is additional source of PA flow. Idealized 3D geometries for Case 1 and Case 2 were created based on the angiograms.

Case 1 consisted of the blood flow through the BGS to the PAs. The simulations were performed for Newtonian and non-Newtonian Carreau viscosity models. Boundary conditions were obtained from Doppler flow velocity studies. Case 2 included a pulsatile blood flow from mBTS an addition to the BGS to the PAs. The simulations were performed using non-Newtonian Carreau viscosity model with specified boundary conditions obtained from cardiac catheterization data. Two cases were compared and the following conclusions were drawn from the results,

1. Wall shear stress increases on the PA walls to thrombogenic levels by including the mBTS with the BGS.
2. The addition of the mBTS significantly increases the pressure in the BGS which may effect celebral blood flow.
3. The mBTS gives rise to vortices on the LPA walls. These vortices are the reason of high wall shear stresses on the LPA walls and as they propagate to the RPA the wall shear stresses decrease. The high wall shear stress gradients on the PA walls are the main sources of the power loss.

4. The additional blood flow through the mBTS increases volumetric flow rates in the LPA and RPA which provides the pulmonary artery growth when the BGS alone is insufficient to maintain it.

7 Recommendations

This work assumes that both the LPA and RPA are laid in a single plane in order to create an idealized model and have a fundamental understanding of the effects of the additional pulsatile blood flow through the modified Blalock-Taussig shunt on the wall shear stress at the pulmonary artery walls. One could create fully 3D geometry in order to take into consideration effects of the curvature of the pulmonary arteries on the flow distribution.

There are several other ways to supply additional pulsatile blood flow to the PAs such as antegrate flow from the right ventricle or connecting the mBTS to the BGS instead of directly connecting it to the LPA. The results could provide doctors an additional insight for choosing the best way to supply blood flow to the PAs.

References

[1] Jahangiri, M., Lincoln, C., Shinebourne, EA. Does the modified Blalock-Taussig shunt cause growth of the contralateral pulmonary artery. *The Annals of Thoracic Surgery,* 67(5):1397-9, May 1999.

[2] Dolan, J.M., Kolega, J., Meng, H. High wall shear stress and spatial gradients in vascular pathology: a review. *Annals of Biomedical Engineering,* 41(7):1411-27, July 2013.

[3] Strony, J., Beaudoin, A., Brands, D., Adelman, B. Analysis of shear stress and hemodynamic factors in a model of coronary artery stenosis and thrombosis. *The American Journal of Physiology*, 265(5):1787-96, November 1993.

[4] Baumgartner HR, Sakariassen KS. Factors controlling thrombus formation on arterial lesions. *Annals of NY Academy of Sciences*, 454:162–77, October 1985.

[5] Sakariassen KS, Joss R, Muggli R et al. Collagen type III induced ex vivo thrombogenesis in humans. Role of platelets and leukocytes in deposition of fibrin. *Arteriosclerosis,* 10(2):276–84, March-April 1990.

[6] P A Holme, U Orvim, M. J. A. G. Hamers, N O Solum, F R Brosstad, R M Barstad, and K S Sakariassen. Shear-Induced Platelet Activation and Platelet Microparticle Formation at Blood Flow Conditions as in Arteries with a Severe Stenosis. *Arteriosclerosis, Thrombosis, and Vascular Biology*, 17(4):646-53, April 1997.

[7] Yoshida M, Yamaguchi M, Yoshimura N, et al. Appropriate additional pulmonary blood flow at the bidirectional Glenn procedure is useful for completion of total cavopulmonary connection. *The Annals of Thoracic Surgery*, 80(3):976–81, September 2005.

[8] Ferns, SJ., El Zein, C., Multani, K., Sajan, I., Subramanian, S., Polimenakos, AC., Ilbawi, MN. Is additional pulsatile pulmonary blood flow beneficial to patients with bidirectional Glenn. *The Journal of Thoracic and Cardiovascular Surgery*, 145(2):451-4, February 2013.

[9] Migliavacca, F., De Leval, MR., Dubini, G., Pietrabissa, R. A computational pulsatile model of the bidirectional cavo pulmonary anastomosis: the influence of pulmonary forward flow. *Journal of Biomechanical Engineering*, 118(4):520-8, November 1996.

[10] Huo, Y., Wischgoll, T., Kassab, GS. Flow patterns in three-dimensional porcine epicardial coronary arterial tree Yunlong Huo, Thomas, and Ghassan S. Kassab, *American Journal of Physiology*, 293(5): 2959-70, November 2007.

[11] Rikhtegar, F., Knight, JA., Olgac, U., Kurtcuoglu, V. Choosing the optimal wall shear parameter for the prediction of plaque location-A patient-specific computational study in human right coronary arteries. *Atherosclerosis*, 211(2):445-50, August 2012.

[12] Zhao, X., Liu, Y., Ding, J., Bai, F., Ren, X., Ma, L., Xie, J., Zhang, H. Numerical of bidirectional Glenn shunt with unilateral pulmonary artery stenosis. *Journal of Mechanics in Medicine and Biology,* 14(04):145-56, August 2014.

[13] Gijsen, FJH., Van De Vosse, FN., Janssen, JD. The influence of the non-Newtonian properties of blood on the flow in large arteries: steady fow in a carotid bifurcation model. *Journal of Biomechanics*, 32(6): 601-8, June 1999.

[14] Cho, Y., Kensey, KR. Effects of the non-Newtonian viscosity of blood in a diseased arterial vessel. Part 1: Steady flows. *Biorheology,* 28(3-4):241-62, February 1991.

[15] Autodesk Inventor Professional, 2015.

[16] ANSYS Academic Research, Release 14.5, Help System, ANSYS FLUENT Theory Guide, ANSYS, Inc.

[17] Sanjeev, S., Karpawich, PP. Superior vena cava and innominate vein dimensions in growing children: an aid for interventional devices and transvenous leads. *Pediatric Cardiology*, 27(4):414-19, July-August 2006.

[18] Ciuti, G., Righi, D., Forzoni, L., Fabbri, A., Pignone, AM. Differences between internal jugular vein and vertebral vein flow examined in real time with the use of multigate ultrasound color Doppler. *American Journal of Neuroradiology*, 34(10):2000-4, October 2003.

[19] Patankar, S.V. Numerical Heat Transfer and Fluid Flow. Taylor & Francis. ISBN 978-0-89116-522-4, 1980.

[20] Saffarian, M., Mohammadi, M., Mohammadi, M. Non-Newtonian Shear Thinning Fluid Passing Throw a Duct with Obstacle Using Power Law Model. *Strojniski vestnik-Journal of Mechanical Engineering,* 61(10):594-600, September 2015.

[21] Lashgari, I., Pralits, J., Giannetti, F., Brant, L. First instability of the flow of shear-thinning and shear-thickening fluids past a circular cylinder. *Journal of Fluid Mechanics,* 701:201-27, June 2012.

Appendices

Appendix A

The comparison of velocity profiles at the inlet to the SVC

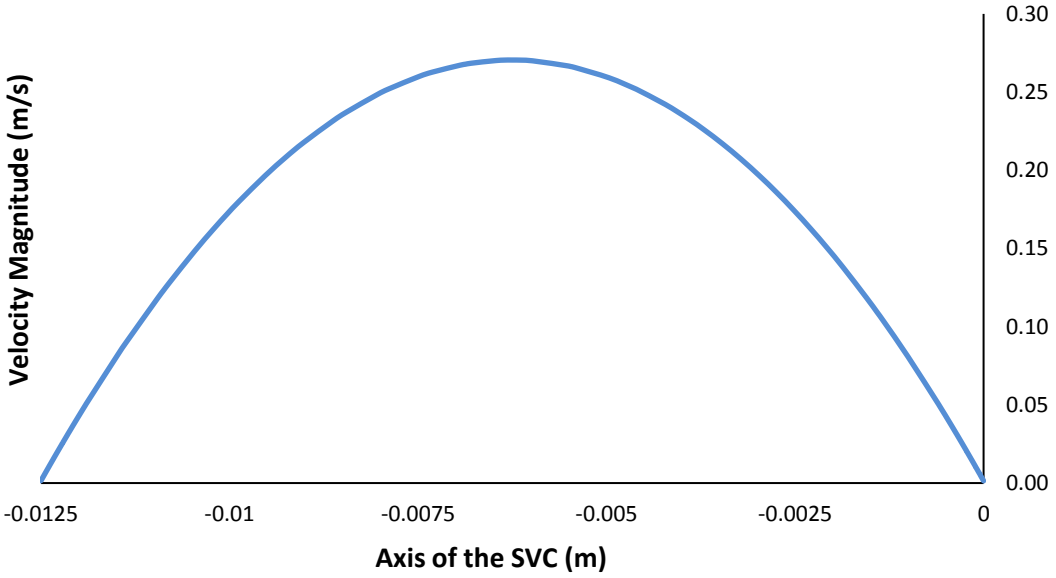

Figure A.1: Parabolic velocity profile at the inlet to the SVC

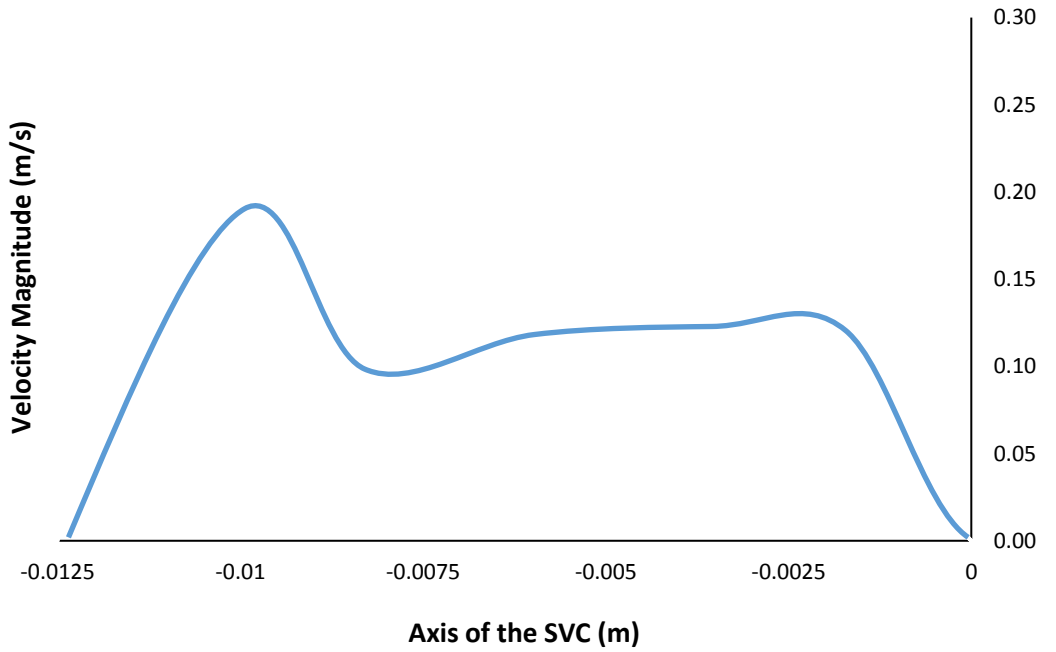

Figure A.2: Velocity profile at the inlet to the SVC in the presence of innominate veins and its branches

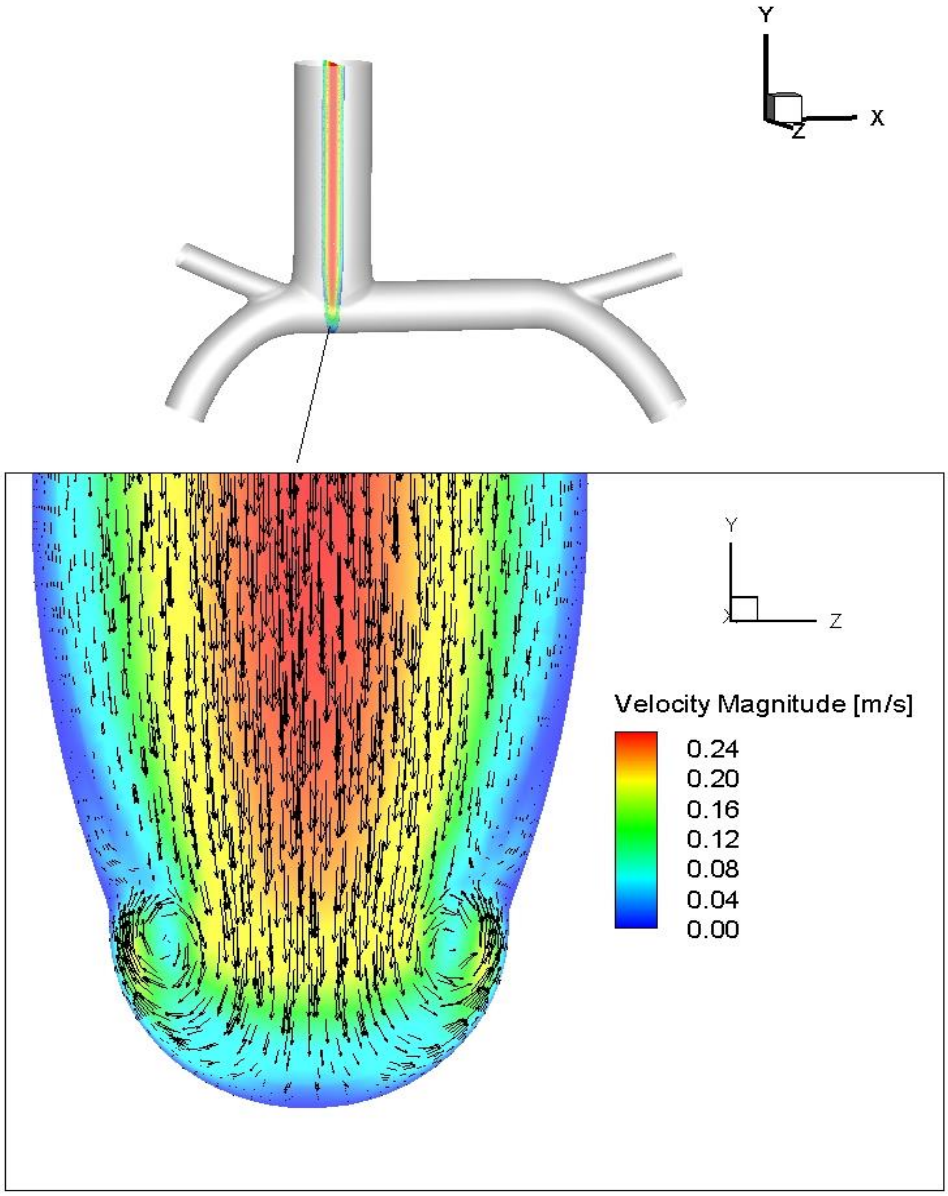

Figure A.3: Contour and vector plot of velocity magnitude at the axis of the BGS when the velocity at the inlet of the SVC is assumed parabolic

Figure A.3 shows the contour and vector plot of velocity magnitude at the axis of the BGS under steady flow conditions using non-Newtonian Carreau viscosity model of blood as a result of assuming parabolic velocity profile at the inlet to the SVC.

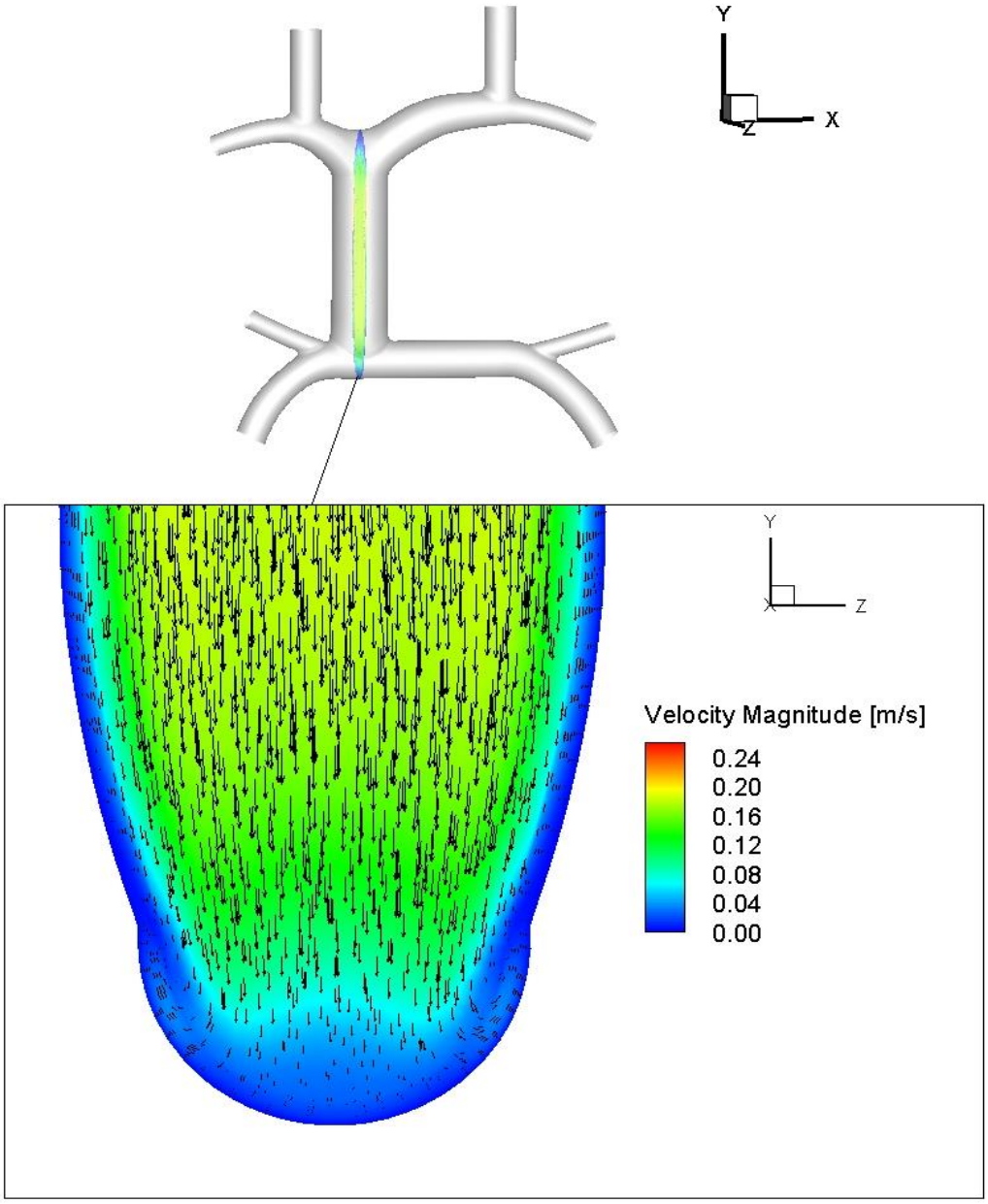

Figure A.4: Contour and vector plot of velocity magnitude at the axis of the BGS when the domain includes innominate veins with the internal jugular and subclavian veins

Figure A.4 shows the contour and vector plot of velocity magnitude at the axis of the BGS under steady flow conditions using non-Newtonian Carreau viscosity model of blood as a result of including the innominate veins with the internal jugular and subclavian veins in order to have a realistic flow in the BGS. At the R-IJV, R-SCV, L-IJV, and L-SCV inlets the parabolic velocity profiles were specified.

Appendix B

Derivation of Energy Loss for Steady and Pulsatile Flow

The energy equation for a control volume may be written as

$$\dot{q}_{in} - \dot{w}_{out} = \frac{\partial}{\partial t}\int_{\forall} e\rho d\forall + \sum_j \int_{A_j} (e + P/\rho)\rho \vec{V}\cdot\vec{n}dA_j \tag{B.1}$$

The second term on the right hand side of Equation (B.1) refers to evaluating the flux integral term at all inlets and outlets. In this term, e is the specific total energy and the sum of the internal, kinetic, and potential energy

$$e = u + \frac{V^2}{2} + gz \tag{B.2}$$

The changes in potential energy between inlet and outlet are negligible. Therefore, the last term on the right hand side of Equation (B.2) is neglected. There is also no work done on or by the control volume, so $\dot{w}_{out}$ is zero and the internal energy is constant over a cross section.

Flow averaged pressure and kinetic energy can be defined as

$$\begin{aligned} \langle P \rangle &= \frac{1}{Q}\int_A P dQ \\ \left\langle \frac{\rho V^2}{2} \right\rangle &= \frac{1}{Q}\int_A \frac{\rho V^2}{2} dQ \end{aligned} \tag{B.3}$$

So that

$$E_{i/o} = \langle P \rangle_{i/o} + \left\langle \frac{\rho V^2}{2} \right\rangle_{i/o} \tag{B.4}$$

Which can be thought of as the rate of energy crossing the boundary per unit volumetric flow rate. Each term in the equation (B.4) has a unit of J/m^3.

Steady Flow

In steady flow the first term on the right hand side of Equation (B.1) is zero. The internal energy term combines with the heat term to produce a steady state of frictional losses converted to heat out of the domain, and represents the net rate of energy loss from inlet to exit, $\Delta \dot{W}_{i-o}$.

For a single inlet and one or more outlets, this becomes,

$$\Delta \dot{W}_{i-o} = E_i Q_i - \sum_j E_{o,j} Q_{o,j} \tag{B.5}$$

The energy efficiency of the system for a steady flow is defined as

$$EE = \frac{\Delta \dot{W}_{i-o}}{E_i Q_i} \tag{B.6}$$

Pulsatile Flow

In the pulsatile flow the rate of energy dissipation is time dependent. The instantaneous rate of change of energy dissipation is written for a single inlet and one or more outlets as

$$\Delta \dot{W}_{i-o} = -\frac{\partial}{\partial t} \int_{\forall} \left(\frac{\rho V^2}{2} \right) d\forall + E_i Q_i - \sum_j E_{o,j} Q_{o,j} \tag{B.7}$$

Equation (B.7) differs from the steady state Equation (B.5) in two respects:

1) There is additional term that represents the instantaneous rate of change in kinetic energy within the volume
2) The flow averaged pressure, kinetic energy, and the flow rates are functions of time.

Tecplot defines ''mass flow weighted average'' of a scalar variable S

$$\bar{S} = \frac{1}{\dot{m}} \int_A S \rho \vec{V} \cdot \vec{n} dA \tag{B.8}$$

$\bar{S}$ is the output from Tecplot. So in Tecplot $S = P$ and $S = \frac{1}{2} V^2$

$$\begin{aligned} \langle P \rangle Q &= \int_A P dQ = \frac{\bar{P}}{\rho} \dot{m} \\ \left\langle \frac{\rho V^2}{2} \right\rangle Q &= \int_A \frac{\rho V^2}{2} dQ = \frac{\overline{V^2}}{2} \dot{m} \end{aligned} \tag{B.9}$$

Note that the definition of the Tecplot average density is incorporated into the definition of the averaged kinetic energy.

Power efficiency

The power efficiency of the system for a fluid flow, averaged over the cardiac cycle is defined as

$$PE = \frac{1}{T} \int \left(1 - \frac{\Delta \dot{W}(t)}{E_i Q_i(t)} \right) dt \tag{B.10}$$

Vita

Seda Aslan was born on January 1, 1991 in Konya, Turkey. She received her bachelor's degree in mechanical engineering from Selcuk University, in 2014. Her graduate career began at the University of New Orleans in 2015. During her graduate years at UNO, she served as a research assistant for Dr. Martin J. Guillot. She completed her master's studies in mechanical engineering at the University of New Orleans in May 2017.